

Deep *Chandra* Observations of NGC 5728: Morphology and Spectral Properties of the Extended X-ray Emission

ANNA TRINDADE FALCAO,¹ G. FABBIANO,¹ M. ELVIS,¹ A. PAGGI,^{2,3} AND W. P. MAKSYM¹

¹*Harvard-Smithsonian Center for Astrophysics,
60 Garden St., Cambridge, MA 02138, USA*

²*Dipartimento di Fisica, Università degli Studi di Torino, via Pietro Giuria 1,
I-10125, Torino, Italy*

³*Istituto Nazionale di Fisica Nucleare, Sezione di Torino, via Pietro Giuria 1,
10125, Torino, Italy*

ABSTRACT

Recent deep *Chandra* observations of nearby Compton thick (CT) AGN have produced surprising results, uncovering extended emission not only in the soft X-rays but in the hard emission (>3 keV), challenging the long-held belief that the characteristic hard X-ray continuum and fluorescent Fe K lines are associated with the torus in the standard picture of AGN. In this work, we present the analysis of our deep (~ 261 ks) X-ray *Chandra* ACIS-S observations of NGC 5728, a nearby ($z=0.00932$) CT AGN. We find that the diffuse emission is more extended at lower energies, in the bicone direction out to ~ 2 kpc radially, but also significantly extended in the direction of the cross-cone, out to ~ 1.4 kpc. Our results suggest that the ratio of detected photons in the cross-cone to the bicone region is $\sim 16\%$, below 3 keV, decreasing to 5% for energies 3-6 keV. The nuclear spectrum suggests a low photoionization phase mixed with a more ionized gas component, while the bicone and cross-cone spectra are dominated by a mix of photoionization and shocked gas emission. A mixture of thermal and photoionization models to fit the spectra indicates the presence of complex gas interactions, consistent with previous observations of other CT AGN (e.g., ESO 428-G014).

Keywords: galaxies: individual (NGC 5728) – galaxies: ISM – galaxies: Seyfert – X-rays: general

1. INTRODUCTION

The interaction between the radiation released by accreting supermassive black holes (SMBHs) in active galactic nuclei (AGN) and the interstellar medium (ISM) is thought to play a crucial role in the evolution of their host galaxies (e.g. [Silk & Rees 1998](#); [Di Matteo et al. 2005](#)). The radiation emitted by the SMBH exists in the form of jets, winds, and outflows and can generate efficient feedback when such interaction initiates a feedback loop that self-regulates star formation and SMBH growth.

In this paper, we analyze the deep *Chandra* observations of the nuclear region of the nearby ($z=0.00932$) active barred spiral, type 2 galaxy NGC 5728, cited as the paradigm of Type 2 AGN with ionization cones by [Urry & Padovani \(1995\)](#) in their review paper on the AGN unification model. At a distance of approximately 41 Mpc ([Mould et al. 2000](#), scale=200 pc/arcsec), NGC 5728 is a CT AGN with a heavily obscured ($\log N_{\text{H}}=24.3$, [Koss et al. 2017](#)) and complex nucleus. In the cross-cone direction, the circumnuclear area exhibits a strong star-forming ring, evident in H II, while it also shows a prominent ionization bicone in the perpendicular direction, as well as a one-sided radio jet ([Wilson et al. 1993](#); [Durré & Mould 2018, 2019](#)). In recent studies, [Durré & Mould \(2018, 2019\)](#) analyzed the spatially-resolved kinematics of the ionized gas in the central region of this galaxy and found that significant amounts of gas ($\sim 38 M_{\odot} \text{ yr}^{-1}$) are being cleared from this area due to the impact of powerful AGN-driven outflows.

Based on the first ~ 19 ks archival *Chandra* ACIS-S image, the X-ray emission in the bicone direction appears extended in the soft band (< 3 keV), a phenomenon that has also been observed in other AGN (e.g., [Wang et al. 2011b](#); [Fabbiano et al. 2018](#)). Similar to the case of the CT AGN ESO 428-G014 ([Fabbiano et al. 2018](#)), extended X-ray emission in the 3-6 keV band is also suggested in the bicone direction. A strong point-like source, absorbed in the soft band, arises at these higher energies. The X-ray

spectrum is a featureless continuum in the 3-6 keV spectral range, and the nuclear source is associated with the strong 6.4 keV Fe-K α line emission in the archival data.

With the cumulative *Chandra* exposure of ~ 261 ks, we reexamined the emission in NGC 5728, aiming at determining the detailed morphological and spectral properties of the extended X-ray emission. Because NGC 5728 is a CT AGN, the X-ray luminosity originating in the nuclear source is heavily attenuated by the torus, and it is not piled up in ACIS-S, allowing us to investigate the circumnuclear region to the smallest sub-arcsecond radii permitted by *Chandra* resolution. The scientific questions we hope to answer for this galaxy all revolve around improving our understanding of AGN-galaxy interaction and feedback. While feedback is an essential component of galaxy evolution, it is only now, with high-quality multi-wavelength data, that a direct observational understanding of the phenomena at play can be obtained.

In this work, we analyze the extended emission in NGC 5728 in the full (0.3-7 keV) energy band observable with *Chandra*. In Section 2, we describe the observations, reduction and analysis of the data, and the alignment procedures applied to these observations. In Section 3, we describe the methods used for the imaging analysis, including modeling of the *Chandra* PSF, and surface brightness radial profiles. Section 4 describes the methods used for the spectral analysis, including the classes of models used to fit the extracted spectra. We then report the final results of our imaging and spectral analysis, both for the extended and the nuclear emission, in Section 5. Finally, in Section 6, we discuss our findings and present our conclusions in Section 7.

2. OBSERVATIONS AND DATA ANALYSIS

NGC 5728 was observed with *Chandra* ACIS-S eleven times, with a total exposure time of 260.8 ks, as shown in Table 1. We retrieved the data from the *Chandra* archive¹, and used CIAO 4.14² to reduce the observations. We reprocessed the data with the standard CHANDRA_REPROCESS script (Fruscione et al. 2006), taking advantage of the sub-pixel capabilities of the ACIS detector due to the spacecraft’s dither; individual observations were astrometrically aligned to the longest observation (ObsID 22582).

Table 1. Details of the used *Chandra* ACIS-S observations and applied offsets.

Obs ID	Date	Exp Time (ks)	P.I.	Applied Offsets (sky pixels)
4077	2003-06-27	18.73	Kraemer	$\Delta x = -0.03$ $\Delta y = 0.77$
22582	2019-12-29	49.42	Fabbiano	ASTROMETRIC REFERENCE
22583	2020-05-22	29.68	Fabbiano	$\Delta x = -0.91$ $\Delta y = -0.51$
23041	2020-04-18	13.89	Fabbiano	$\Delta x = 0.24$ $\Delta y = 1.08$
23042	2021-04-12	25.73	Fabbiano	$\Delta x = 1.06$ $\Delta y = -0.06$
23043	2020-05-12	19.81	Fabbiano	$\Delta x = -0.64$ $\Delta y = -0.17$
23221	2020-04-16	15.86	Fabbiano	$\Delta x = 0.08$ $\Delta y = 0.96$
23249	2020-05-14	29.68	Fabbiano	$\Delta x = -1.09$ $\Delta y = -0.44$
23254	2020-05-23	19.82	Fabbiano	$\Delta x = -1.08$ $\Delta y = 1.09$
25006	2021-04-12	21.79	Fabbiano	$\Delta x = 1.34$ $\Delta y = -0.59$
25007	2021-04-16	16.37	Fabbiano	$\Delta x = 1.00$ $\Delta y = 0.42$

¹ <https://cda.harvard.edu/chaser/>

² <http://cxc.harvard.edu/ciao>

To build the most accurate merged data set, we examined two different ways of aligning the images from different observations. The first approach was to align the observations using the centroids of the images in the 6-7 keV energy band, which has the advantage of being dominated by the nuclear position in CT AGN. To determine the centroid of the nuclear source for each individual observation, we built images in the 6-7 keV energy band, with subpixel scale of 1/8 of the native ACIS pixel (smoothed with a 2D Gaussian kernel with $\sigma=2$), selecting the brightest pixel in the output image. We used `DMSTAT` to calculate the centroid of the count distribution within a circle of radius $r=0.2''$, centered on the brightest pixel of the smoothed image. We then used the tool `WCS_UPDATE` to apply the offsets, with shifts input to the `DELTA X` and `DELTA Y` parameters in units of sky pixels (Table 1). Finally, we used the new aspect solution to re-calculate the World Coordinate System (WCS) events positions in the original event file with the `REPROJECT_OBS` tool.

We confirmed the accuracy of our results by evaluating off-nuclear point sources in the field of view ($<8''$ away from the active nucleus). We used `WAVDETECT`, with $\sqrt{2}$ scales³ adopted as the wavelet parameter and a significance threshold of 10^{-6} false detections per pixel. By comparing the offsets of the detected point sources centroids in the single observations relative to the final merged image (in the 0.3-7 keV band), we found that this method yields nuclear positions consistent with those found by aligning the image centroids in the 6-7 keV energy band.

To identify fainter emission features, we created a merged event file using `MERGED_OBS`. The reprojected images of individual observations and the merged image are shown in Fig. 1. These are $20'' \times 15''$, 1/8 subpixel images, smoothed with 4 pix Gaussian, in the 0.3-7 keV energy band.

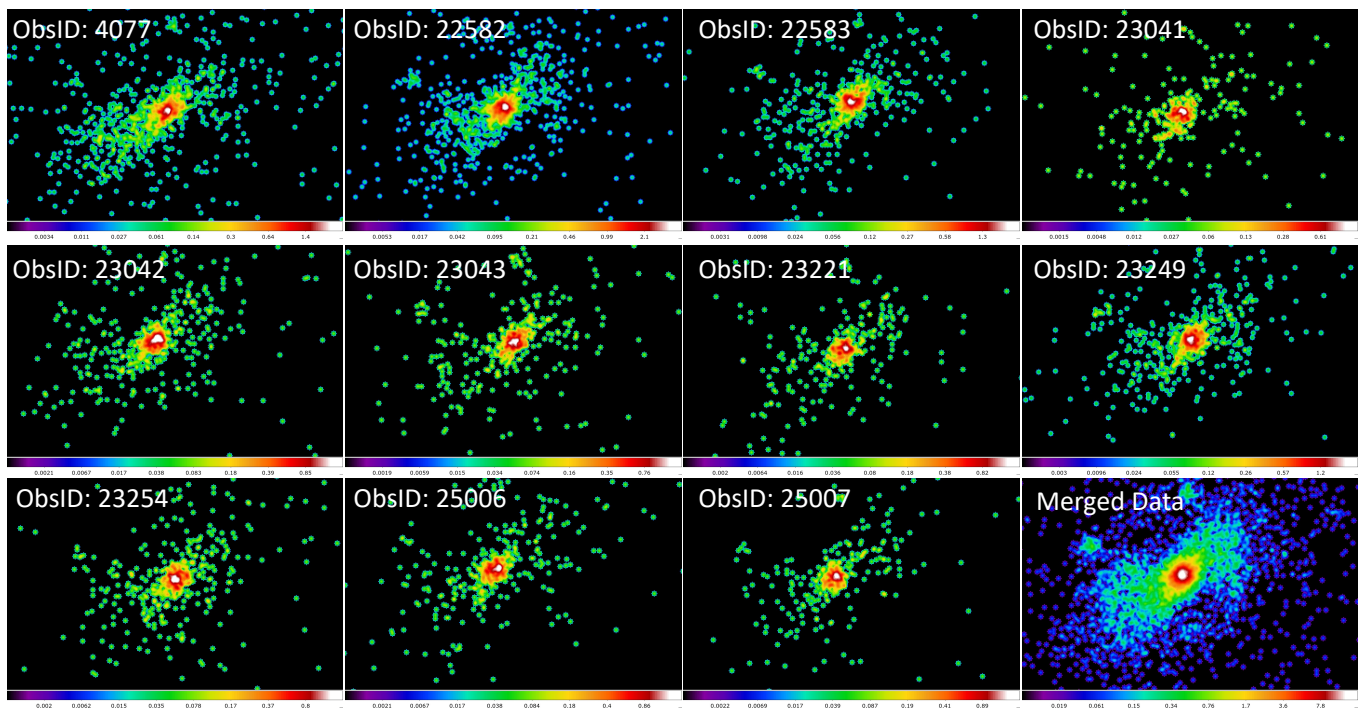


Figure 1. 1/8 subpixel 0.3-7 keV images of all observations plus the final merged image (bottom right panel), which was obtained by aligning all eleven images. N is up, and E is to the left. All panels are $20'' \times 15''$ in size. Images were smoothed with 4 pixel Gaussian.

³ With 1.0, 1.4, 2.0, 2.8, 4.0, 5.7, 8.0, 11.3, 16.0, used to get a more extensive run.

3. IMAGE ANALYSIS

3.1. *Chandra PSF Modeling*

Following *Chandra* science threads⁴, we simulated the point spread function (PSF) of all individual observations listed in Table 1. To do so, we used CHART⁵, taking into account the corresponding individual source spectrum (extracted with SPEXTRACT⁶), aspect solution, and off-axis angle as inputs for the simulations. We then projected the PSF rays onto the detector plane with MARX, taking into account the nominal position of the detector during the observation, the observation date, and the exposure time. We also set the appropriate telescope and detector configuration and corrected for science instrument module (SIM) offset. To avoid any effects due to pixelization, we set conservatively ASPECTBLUR=0.2⁷, as recommended in MARX for ACIS-S observations. Each CHART simulation was individually projected and made into event files, which were then combined into a single event file using DMERGE. We used ObsID 22582 as our astrometric reference to merge the PSF models, and the final PSF event file was normalized to the source counts within a circle of 0.5'' radius.

3.2. *Probing the Extended X-ray Emission*

The final full-band image of NGC 5728 is shown in more detail in Fig. 2. The upper-left panel shows the "raw" 1/8 subpixel merged image, while the lower-left panel shows the 1/8 subpixel merged image smoothed with 4 pix Gaussian. The right panel shows the merged image adaptively smoothed with Gaussian (0.5-30 pix scales, 10 counts under the kernel, 60 iterations). This image shows a prominent point-like nuclear source and fainter X-ray emission extended $\sim 10''$ (~ 2 kpc) radially from the nucleus, in the SE-NW direction, which is also the direction of the ionization bicone (Durré & Mould 2018).

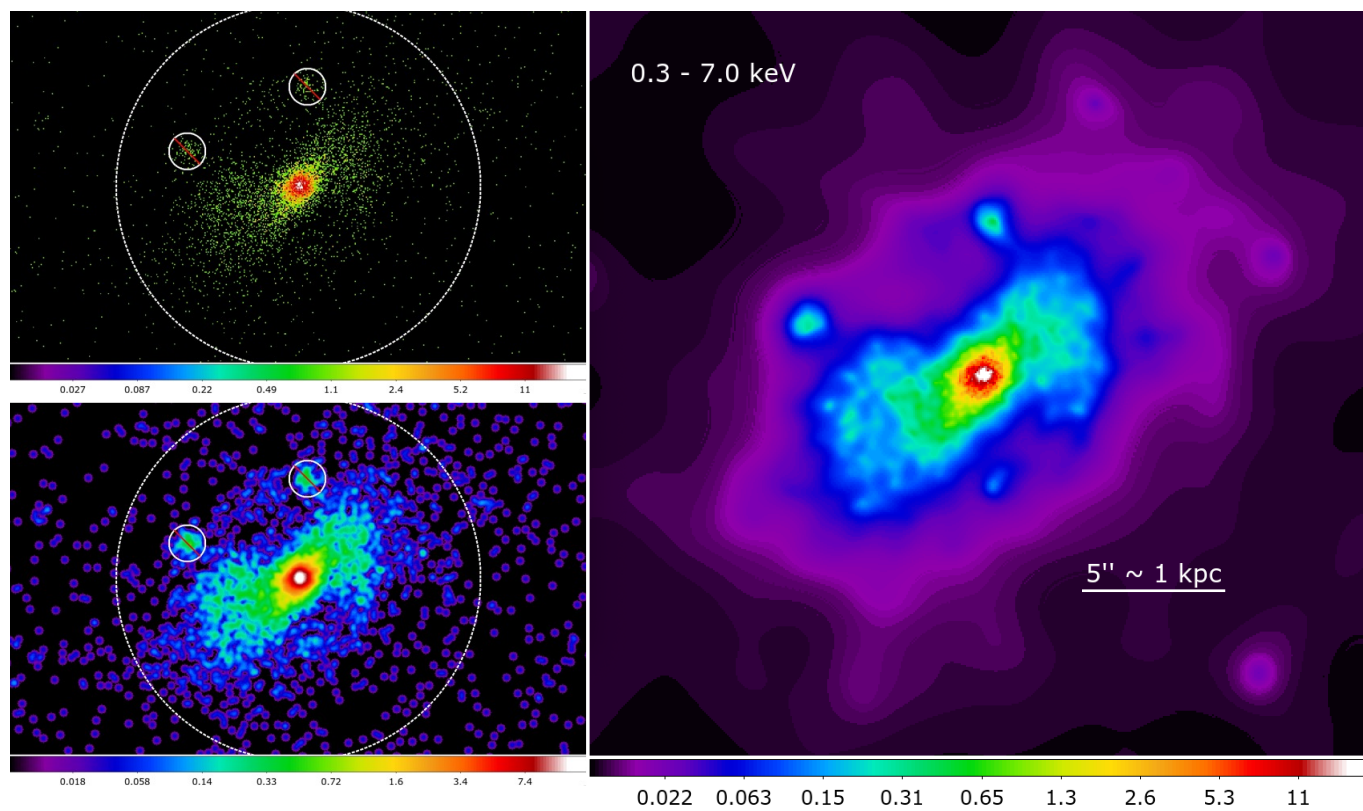


Figure 2. Emission in the full-band (0.3-7 keV). **Top-Left:** "raw" 1/8 subpixel merged image. **Bottom-Left:** 1/8 subpixel merged image smoothed with 4 pix Gaussian. **Right:** merged image adaptively smoothed with Gaussian (0.5-30 pix scales, 10 counts under the kernel, 60 iterations). The regions of non-nuclear point sources excluded from the spectral analysis and surface brightness profiles are marked. Dashed circles have a radius of $10''$ (~ 2 kpc).

⁴ <https://cxc.cfa.harvard.edu/ciao/threads/>

⁵ <https://cxc.harvard.edu/ciao/PSFs/chart2/>

⁶ https://cxc.cfa.harvard.edu/ciao/threads/marx_sim/

⁷ <https://cxc.cfa.harvard.edu/ciao/why/aspectblur.html>

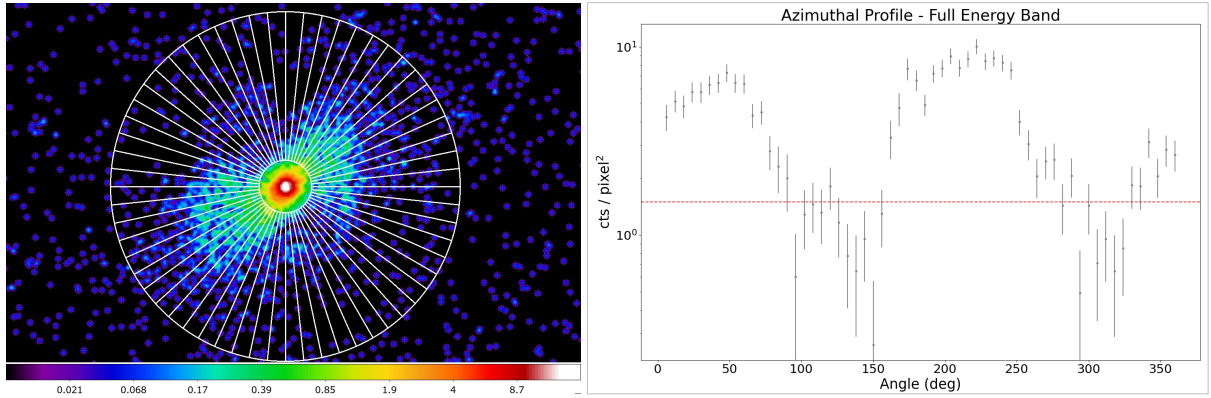


Figure 3. *Left:* *Chandra* full energy band image with overlaying $1.5''$ – $10''$ annular extraction region used to extract the azimuthal profile from the merged data (60 angular bins of 6°). *Right:* Merged data azimuthal profile (in gray). The red horizontal line indicates 1.5 counts/pixel².

We sliced the final merged image in bicone and cross-cone sectors to investigate each region’s circumnuclear gas morphology and extent separately. To optimally determine the angles of these regions, we produced a surface brightness azimuthal profile of the 0.3–7 keV merged image within the $1.5''$ – $10''$ annular region centered on the nucleus, with angular bins of 6° (Fig. 3). The profile obtained was fitted with two Gaussians plus a constant to account for the background level. Based on the Gaussian centers and widths, we selected the bicone angles to be: NW cone between 336° and 90° (measured counter-clockwise from north), and the SE cone between 162° and 270° . Similarly, the cross-cone angles are defined as: NE cross-cone between 90° and 162° , and SW cross-cone between 270° and 336° , as shown in Fig. 4, 5, and 6 (leftmost column).

To quantify the magnitude and significance of the extended components in different energy bands, we energy-filtered the merged event file and the merged *Chandra* PSF model, following *Chandra* threads⁸ to extract the surface brightness profile of both data sets. We used `wavdetect` to identify off-nuclear point sources in the final merged image, excluding these from the radial profiles, as shown in Fig. 2. The rightmost columns in Fig. 4, 5, and 6 show a comparison between the radial surface brightness profiles of the merged image (in black) and merged model PSF (in red), in different energy bands in the cone and cross-cone directions. The data and PSF radial surface brightness profiles were extracted from $1/8$ subpixel images, with bin sizes varying to contain a minimum of 10 counts per bin in the image data set. Because the model PSF was built to match the cumulative exposure time of the data, the noise observed in the radial profiles is consistent with statistical noise. The gray horizontal line indicates the level of the field background derived from the same image as the profiles. Since the profiles are background subtracted, points below the background level are valid data. Outside the plotted range, the profiles are dominated by noise.

Table 2. Excess Data Counts over Model PSF for $1.5''$ – $8''$ Conical Regions.

Energy (keV)	NW Cone Sector	SE Cone Sector	Cross-Cone Sectors
	Excess (error)	Excess (error)	Excess (error)
0.3-7.0	1189 (34)	1216 (35)	324 (18)
0.3-1.5	466 (22)	605 (25)	215 (15)
1.5-3.0	421 (21)	376 (19)	78 (9)
3.0-4.0	132 (11)	83 (9)	18 (4)
4.0-5.0	75 (9)	67 (8)	10 (3)
5.0-6.0	32 (6)	42 (7)	3 (2)
5.8-6.2	21 (5)	25 (5)	6 (3)
6.0-7.0	63 (7)	43 (6)	-
6.1-6.6	43 (6)	32 (6)	-
6.7-7.2	8 (3)	16 (4)	3 (2)

⁸ https://exc.cfa.harvard.edu/ciao/threads/radial_profile/

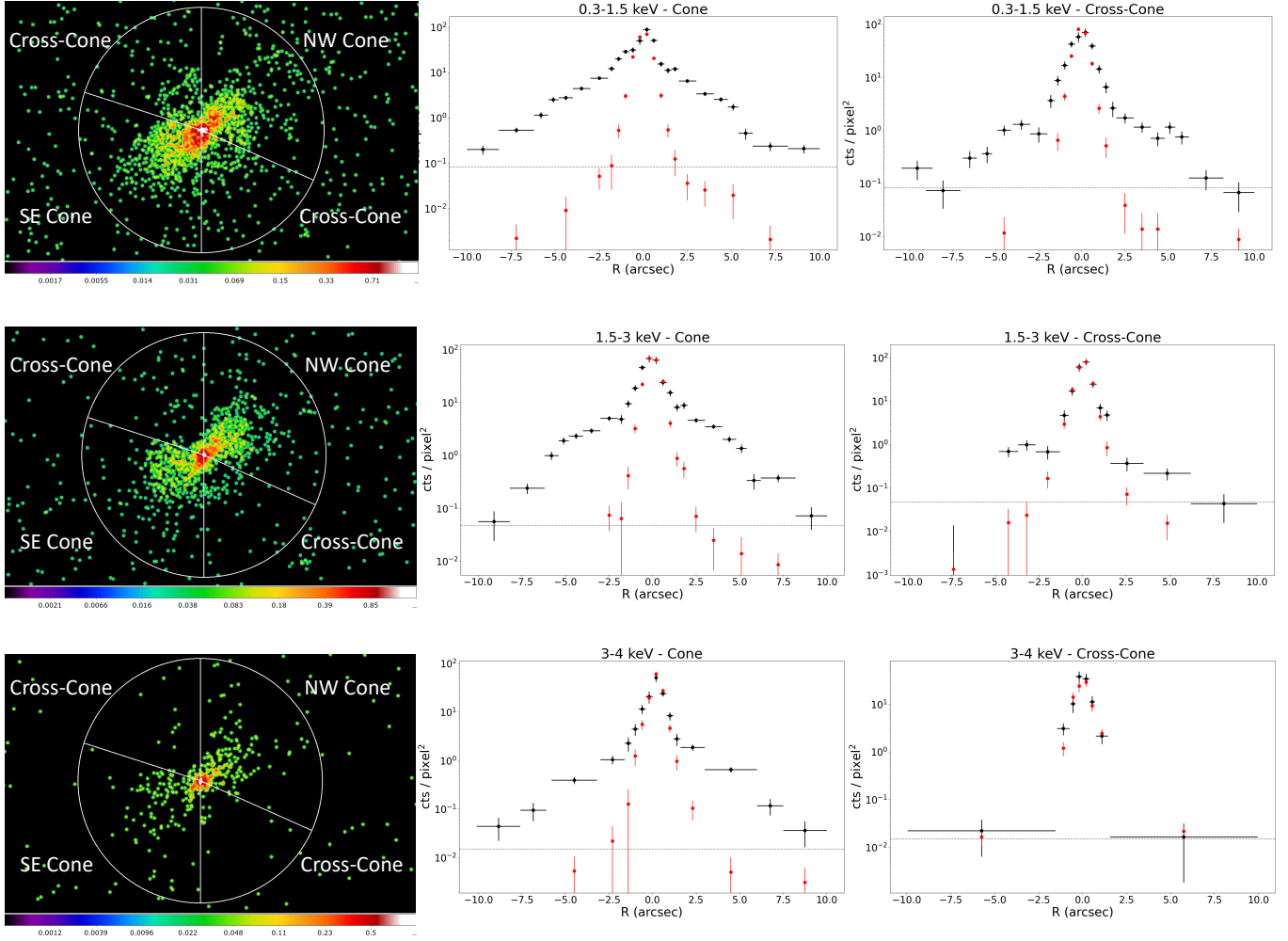


Figure 4. Images (leftmost column), and background-subtracted surface brightness radial profiles in the bicone (middle column) and cross-cone (rightmost column) sectors of NGC 5728 in different energy bands (top panels: 0.3–1.5 keV; middle panels: 1.5–3 keV; bottom panels: 3–4 keV). The images were re-binned at 1/8 of native pixel and smoothed with Gaussian (setting the following parameters: radius = 4, sigma = 2, in pixels). The PSF in the same energy band was normalized to the source image in the central $0.5''$ circle. The bin size was chosen to contain a minimum of 10 counts in the image data set (extraction regions with less than 10 counts were not plotted). The dashed gray horizontal line indicates the level of the field background for each plot.

4. SPECTRAL ANALYSIS

Based on the cone and cross-cone profiles obtained in Section 3, we selected four regions from which to extract the spectral data: (1) a $1.5''$ -radius circle to properly encompass the nuclear emission and the surrounding inner circumnuclear emission; two annuli of $1.5''$ - $8''$ radius centered on the nucleus, which do not encompass the central emission region, we name (2) northwest (NW) cone, (3) southeast (SE) cone, and two sectors of $2.5''$ - $8''$ annulus we name (4) cross-cone⁹ (Fig. 7). Previous radio and optical studies of a different CT AGN, IC 5063, have shown that the two cone regions can host multiphase gas with different properties, e.g., density and kinematics (Morganti et al. 2007; Dasyra et al. 2016). Taking this into account, we separately analyzed the spectral properties of the NW and SE cones, to account for any differences between the two locations.

We used CIAO SPECEXTRACT to extract the spectra from individual observations. All spectra were background subtracted from a circular region of $10''$ radius, free of X-ray point-like sources. The eleven individual spectra and responses were co-added using

⁹Based on the radial profiles, there is no hard extended emission in the cross-cone direction (> 4 keV). Therefore, to avoid any emission from nuclear spillover, we opt to use a $2.5''$ - $8''$ annulus for the cross-cone emission spectral extraction.

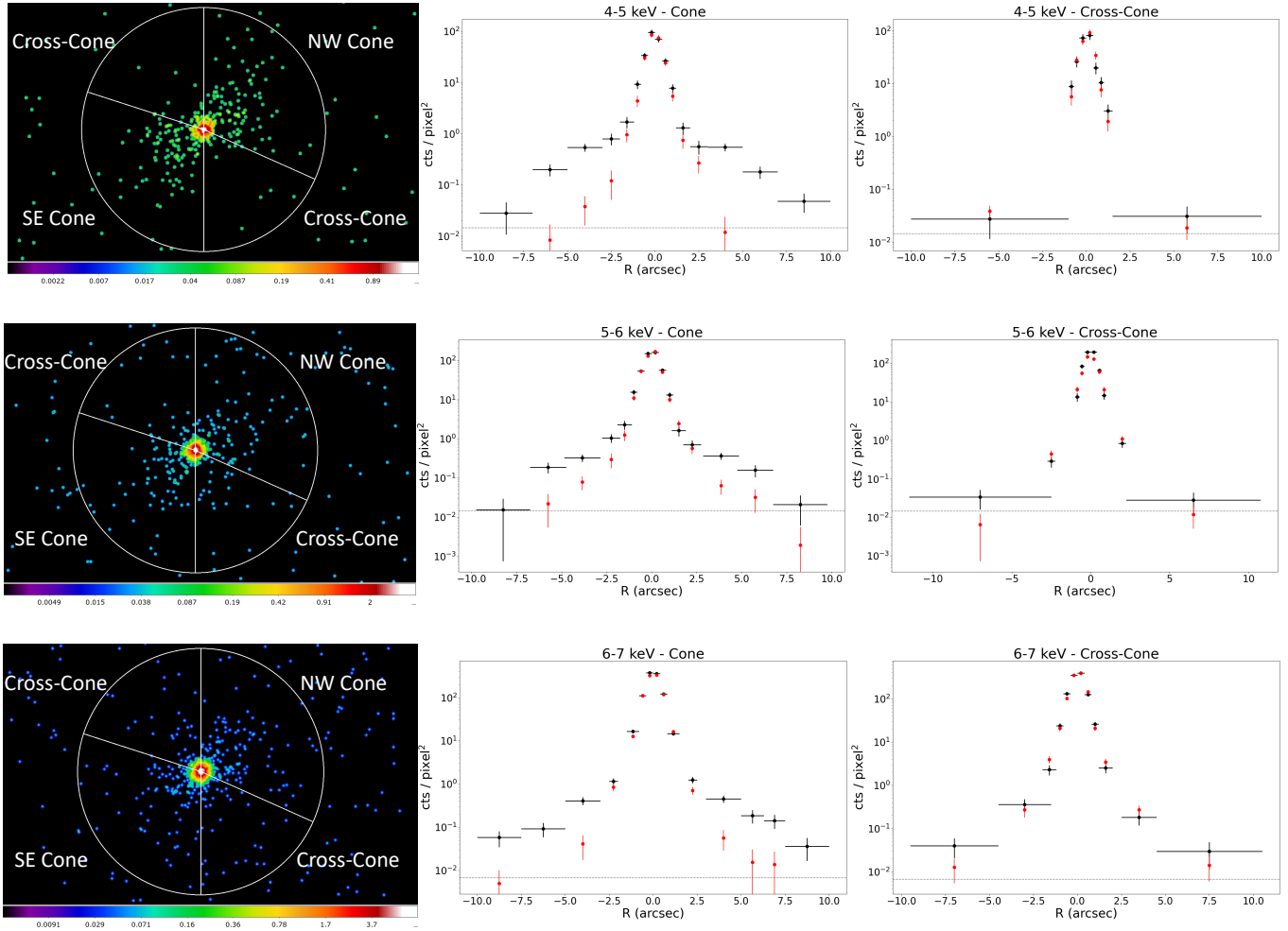


Figure 5. Top row: 4–5 keV; middle row: 5–6 keV; bottom row: 6–7 keV. See the caption in Fig. 4 for details.

the `COMBINE_SPECTRA`¹⁰ script and binned to have a minimum of 20 counts bin^{-1} , to allow for a reliable χ^2 fitting. We then used `SHERPA`¹¹ (Freeman et al. 2001) to fit the final merged source spectrum.

4.1. Spectral Modeling

Following previous works (e.g., Fabbiano et al. 2018; Paggi et al. 2022), we adopted two classes of models to describe the spectra extracted from the different regions:

PHENOMENOLOGICAL MODELS:

This class of models is used to locate the spectral regions of line emission in each extracted spectra. In addition to the photo-electric absorption by the Galactic column density along the line of sight ($N_H = 7.53 \times 10^{20} \text{ cm}^{-2}$, derived with the `NASA HEASARC` tool¹²), these models comprise a power-law with variable photon-index and several red-shifted Gaussian lines with widths free to vary (requiring $\sigma \geq 0.1 \text{ keV}$, the `ACIS-S` instrument energy resolution). The redshift assumed for the emission lines is systemic only ($z = 0.00932$), and an intrinsic absorption component was included in the models when necessary.

Table 5 (in Appendix) lists the results of the spectral fits for the phenomenological models, including the best-fit energies of the emission lines¹³. The total flux of the best-fit model is also shown. We note that these models should not be used to infer any

¹⁰ https://cxc.cfa.harvard.edu/ciao/ahelp/combine_spectra.html

¹¹ <https://cxc.cfa.harvard.edu/sherpa/>

¹² <https://heasarc.gsfc.nasa.gov>

¹³ We opt to move Table 5 to the Appendix to maintain the flow of the paper

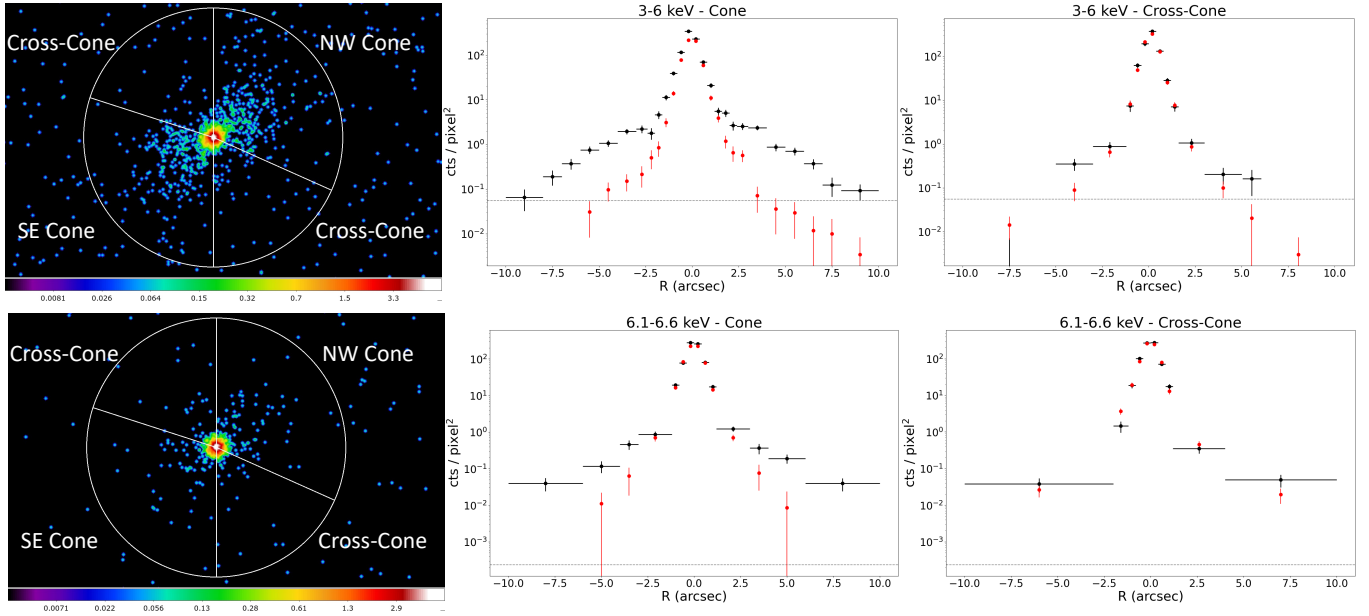


Figure 6. Same as in Fig. 4, for 3-6 keV (top) and the Fe $K\alpha$ band (bottom).

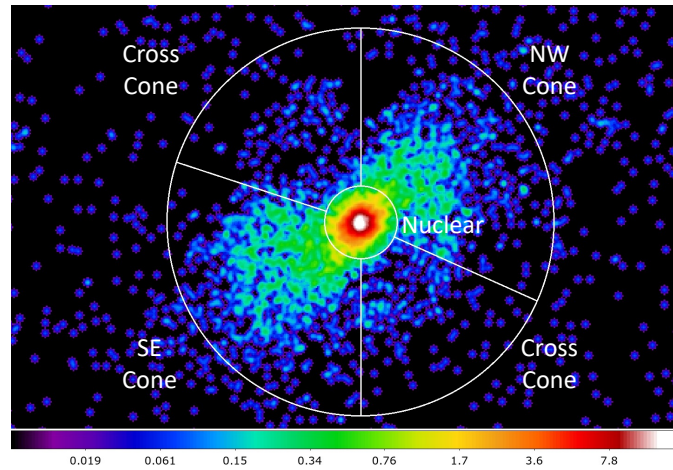


Figure 7. 1/8 pixel image of the emission in the 0.3–7 keV band. White solid lines divide the nucleus of NGC 5728 from the extended ($>1.5''$) region, which, in turn, is split into four regions to separate the bicone from the cross-cone area, as shown. Specifically, the bicone regions are enclosed in northwest (NW) and southeast (SE) sectors and limited at the position angles 336° - 90° and 162° - 270° , respectively. The off-nuclear point sources have been removed for the spatial and spectral analysis, as shown.

"physical" processes and line fluxes, especially in the range < 1.5 keV, where several blended emission lines cannot be entirely spectrally resolved at ACIS resolution.

PHYSICAL MODELS:

We use this class of models to probe possible physical emission mechanisms in each extraction region. The extracted spectra were fitted with photoionization (CLOUDY¹⁴) (Ferland et al. 2017) and thermal (APEC¹⁵) (Foster et al. 2012) models, as well as combinations of both (CLOUDY+APEC models). In all the fits, the model includes the best-fit nuclear continuum and Fe $K\alpha$ line model from Table 5. We started with one-component models and added additional components to improve the fit quality. We

¹⁴ <http://www.nublado.org/>

¹⁵ <http://www.atomdb.org/>

also grouped the best-fit residuals to identify cases in which we obtain overall formally good fits (i.e. reduced $\chi^2 \sim 1$) but have significant residuals in certain energy bands, to which χ^2 is not sensitive. We used these inspections to justify the addition of a new component to the model.

1. Photoionization

We built grids of models with the `CLOUDY` c17.03 package for the photo-ionization components. Assuming a continuum source with a spectral energy distribution (SED) in the form of a power law $L_\nu \propto \nu^{-\alpha}$, with $\alpha = 1.0$, for $1 \times 10^{-4} \text{ eV} < h\nu < 13.6 \text{ eV}$, $\alpha = 1.3$, for $13.6 \text{ eV} < h\nu < 500 \text{ eV}$, and $\alpha = 0.5$, for $500 \text{ eV} < h\nu < 30 \text{ keV}$, with exponential cutoffs above and below the limits (e.g., Kraemer et al. 2020). The grids of models obtained also depend on the choice of input parameters, i.e., the radial distance of the photoionized gas to the central AGN (r), the column density (NH), and the number density (n_H), being parameterized in terms of the ionization parameter, U .

Concerning element abundances for these models, we consider 1.4x solar abundances. Specifically (in log, relative to hydrogen, by number): He=-1.00, C=-3.47, N=-3.92, O=-3.17, Ne=-3.96, Na=-5.69, Mg=-4.48, Al=-5.53, Si=-4.51, S=-4.82, Ar=-5.40, Ca=-5.64, Fe=-4.4, and Ni=-5.75 (e.g. Trindade Falcão et al. 2021a; Kraemer et al. 2020).

The grid of `CLOUDY` models was built over a range of NH and U (varying in the range $\log U = [-2.00 : 3.00]$ in steps of 0.1, and the hydrogen column density NH, expressed in cm^{-2} , varying in the range $\log \text{NH} = [20.0 : 23.5]$ in steps of 0.1). We assumed a turbulence velocity of 100 km s^{-1} (e.g., Armentrout et al. 2007; Kraemer et al. 2020). The `CLOUDY` output was converted onto additive emission components (ATABLES) in a FITS format (Porter et al. 2006), with `SHERPA` interpolating between the values in the grid in the fitting process.

2. Thermal

The thermal plasma was represented by `APEC` models with solar abundances. The model predicts line and continuum emissivities for an optically thin, hot plasma, using the AtomDB atomic database to calculate an emission spectrum from a collisionally-ionized diffuse gas. The modeled optically thin emission can result from thermalized ISM after being collisionally ionized via interactions with winds or radio jets from either the nuclear source or the very prominent star-forming ring.

3. Photoionization + Thermal Models

To investigate models that would give a better fit over the entire spectral range, we tried a set of mixed photoionization and thermal models (in addition to the nuclear continuum model). These included an increasing number of photoionization components (from 1 to 3) plus a thermal component and an increasing number of thermal components (from 1 to 3) plus a photoionization component. We also try a 2-photoionization + 2-thermal model.

5. RESULTS

5.1. X-ray Morphology

As shown in Figure 4, the soft 0.3-1.5 keV band is the most extended. Comparison with the PSF profiles shows that the surface brightness in this energy band is extended in both cone and cross-cone directions, although the extent in the cross-cone direction is smaller. In the cone direction, the surface brightness can be traced to $\sim 10''$ ($\sim 2 \text{ kpc}$) radially and up to $\sim 7''$ (1.4 kpc) in the cross-cone direction. In the 1.5-3.0 keV band, emission can be traced to $\sim 10''$ (2 kpc) radially, in the cone direction, and up to $\sim 6''$ (1.2 kpc) in the cross-cone, in excess of the respective model PSF profiles.

Fig. 6 (top) shows the cone and cross-cone profiles for the 3-6 keV band, which contains 567 ± 24 net source counts within a $1.5''\text{-}8''$ radius annulus, after excluding the off-nuclear point sources in the field. There are ~ 462 counts in excess of what could originate from a nuclear point source (Table 2). The surface brightness in this energy band extends radially to $\sim 10''$ (2 kpc) in the cone direction; therefore, this continuum emission cannot be directly attributable to the emission from the immediate vicinities of the central active nucleus. The extent of the surface brightness decreases at higher energies and in the cross-cone direction. In all cases, the emission in the cone direction is more extended than that of the PSF in the same energy band, but it is consistent with the PSF for energies 3-6 keV in the cross-cone direction.

In Fabbiano et al. 2017, the authors reported the discovery of kpc-scale diffuse emission in both the hard continuum (3-6 keV) and in the Fe $K\alpha$ line band in ESO 428-G014, another CT AGN. Fig. 6 (bottom) shows the imaging cone and cross-cone X-ray emission and surface brightness radial profiles in the 6.1-6.6 keV band for NGC 5728. As shown, this emission is extended in the cone direction, $\sim 6''$ (1.2 kpc), while it is consistent with the PSF in the cross-cone.

In summary, radial profiles and images reveal kpc-scale emission at energies $< 3 \text{ keV}$, which are dominated in X-rays by line emission (see Section 4), and in the 3-6 keV continuum and Fe $K\alpha$ line energy bands. While this extent is more pronounced in the cone direction, which is the direction of the ionization bicone, the emission is also extended in the "cross-cone" direction at energies up to $\sim 3 \text{ keV}$.

Table 3. Best Physical Parameters of the Photo-ionized and/or Collisionally-ionized Gas in All Regions

Region	Best-fit Model	Model Energy Flux* (0.3-7.0 keV; in erg/cm ² /s)	Reduced χ^2	d.o.f.	Alternative Model Components	Reduced χ^2	d.o.f.
(1.5'' circle)	log(NH1)=20.4±0.1 log(NH2)=23.3±0.5 log(U1)=0.4±0.1 log(U2)=-1.6±0.1	6.8×10 ⁻¹³	0.68	213	log(NH1)=20.3±0.1 log(NH2)=23.3±0.4 log(U1)=0.4±0.1 log(U2)=-1.6±0.1 kT 1=1.4±0.2 EM1=2.1×10 ⁻⁶	0.67	211
	log(NH1)=21.1±0.1 log(NH2)=20.5±0.1 log(U1)=1.7±0.1 log(U2)=0.4±0.1 kT 1=0.6±0.15 kT 2=1.4±0.27 EM1=1.5×10 ⁻⁶ EM2=1.8×10 ⁻⁶				log(NH1)=21.2±0.12 log(NH2)=20.6±0.12 log(U1)=1.6±0.1 log(U2)=0.3±0.10		
(NW Bicone Region)	log(NH1)=21.7±0.1 log(U1)=-0.9±0.08 kT 1=0.8±0.11 kT 2=1.3±0.11 EM1=5.3×10 ⁻⁶ EM2=1.6×10 ⁻⁶	1.0×10 ⁻¹³	0.94	60	log(NH1)=21.7±0.1 log(NH2)=21.7±0.1 log(U1)=-0.9±0.10 log(U2)=0.5±0.11 kT 1=0.8±0.12 kT 2=1.4±0.12 EM1=5.4×10 ⁻⁶ EM2=1.6×10 ⁻⁶	0.98	57
	log(NH1)=21.7±0.1 log(U1)=-0.9±0.08 kT 1=0.8±0.11 kT 2=1.3±0.11 EM1=5.3×10 ⁻⁶ EM2=1.6×10 ⁻⁶				log(NH1)=21.7±0.1 log(NH2)=21.7±0.1 log(U1)=-0.9±0.10 log(U2)=0.5±0.11 kT 1=0.8±0.12 kT 2=1.4±0.12 EM1=5.4×10 ⁻⁶ EM2=1.6×10 ⁻⁶		

U is the ionization parameter of each component

NH is the column density (cm⁻²) of each component

kT is the temperature (keV)

EM is the normalization of the APEC model, which is proportional to the emission measure.

* Calculated using the CALC_ENERGY_FLUX tool on SHERPA. It represents the integral of the unconvolved model over the 0.3-7 keV energy band.

5.2. Spectral Properties

We characterized the spectral properties of the extended and nuclear X-ray emission in NGC 5728. The results of our detailed analysis are shown below for each extraction region.

5.2.1. The Nuclear Emission

The nuclear spectrum (1.5'' circle) exhibits both strong hard (>3 keV) and soft X-ray emission at lower energies. We fit the hard emission by employing a nuclear model that includes three components: (i) one component to account for the SMBH emission transmitted through the dusty torus, (ii) one component to account for the reflected SMBH emission (due to Compton scattering) from the torus, and (iii) one model component to account for the 6.4 keV Fe K α emission line. In addition, we employed additional spectral components to model the soft excess, as described below (e.g., Krolik et al. 1994).

We used SHERPA to describe the AGN spectrum using the following set of models. The emission from the SMBH was assumed to follow a power law with a high-energy cutoff, modeled with XSCUTOFFPL. The cutoff energy in AGNs is usually above 150 keV, but for this study we fixed it at 200 keV (Semena et al. 2019). The absorption of the emission in the torus was modeled using the XSZTBABS model. The reflected emission was described using the XSPEXRAV spectral model, which is a semi-analytical model of the spectrum produced when an isotropic X-ray emission is reflected from a plane layer of cold, non-ionized gas with infinite optical depth (Magdziarz & Zdziarski 1995). The observer's angle to the plane layer was assumed to be $\cos\theta = 0.5$, and the iron abundance in the layer was set to be solar. The cutoff energy in the incident emission spectrum E_{cut} was linked to that of the reflected emission. To model the fluorescent iron line (Fe K α), we used one gaussian with fixed line position at 6.41 keV, given the AGN redshift. In SHERPA terminology, our model for the hard spectrum is expressed as XSTBABS × [XSPEXRAV + XSZTBABS × [XSCUTOFFPL] + XSZGAUSS]. As for the soft emission, we fit the observed soft excess with a simple absorbed power law (XSPOWERLAW).

The best-fit model yields a soft power-law component, a hard power-law component, and a reflection component with photon indexes $\Gamma = 1.5 \pm 0.2$, $\Gamma = 1.8 \pm 0.1$, and $\Gamma = 1.8 \pm 0.1$, respectively. The estimated column density absorption is $N_H \sim 1.0 \pm 0.1 \times 10^{24} \text{ cm}^{-2}$, which is consistent with the findings of [Shu et al. \(2007\)](#) and [Semena et al. \(2019\)](#) for this galaxy.

There are a total of nine fitted emission lines, including neutral Fe $K\alpha$ emission with an equivalent width $EW=0.77 \text{ keV}$, similar to that found in previous works (e.g., [Semena et al. 2019](#); [Tanimoto et al. 2022](#)). Table 5 gives the best-fit parameters and the energies of the fitted emission lines.

The nuclear spectrum shows emission to the left ($\sim 6.1 \text{ keV}$) and to the right ($\sim 6.7 \text{ keV}$) of the neutral Fe $K\alpha$ line, which our phenomenological fit did not pick up, as well as a Fe edge absorption feature at 7.1 keV . Below 3 keV , the most prominent feature is at $\sim 1.8 \text{ keV}$, which we associate with a blend of Mg XII, Si XIII, and Fe XXIV transitions. For comparison, we fit the hard ($> 3 \text{ keV}$) nuclear spectrum with a second physically motivated model, `BORUS02` ([Baloković et al. 2018](#)), which also incorporates hard ($> 8 \text{ keV}$) constraints. Our results show that the excess emission observed to the left and to the right of the neutral Fe $K\alpha$ line are roughly identical, compared to the results obtained using `PEXRAV`, suggesting these features to be model-independent. We present the details of this analysis in the Appendix (Fig. 16).

Multi-component models combining photoionization and/or optically thin thermal models show that the soft nuclear emission is dominated by a high photoionization ($\log U \sim 0.4$), low column density ($\log N_H \sim 20.3 \text{ cm}^{-2}$) gas component, which allows us to reproduce prominent emission lines at $\sim 1.8 \text{ keV}$ and $\sim 2.3 \text{ keV}$. A second, low-photoionization component ($\log U \sim -1.6$), with high column density ($\log N_H \sim 23.3 \text{ cm}^{-2}$) models the soft excess emission (Fig. 8). Best fit parameters for chosen models are given in Table 3.

We do not find any evidence that suggests the need for a thermal component to fit the nuclear spectrum. In fact, as shown in Fig. 8, the addition of a 1-thermal component to a 2-photoionization model does not modify the residuals or reduced χ^2 of the fit (Table 3).

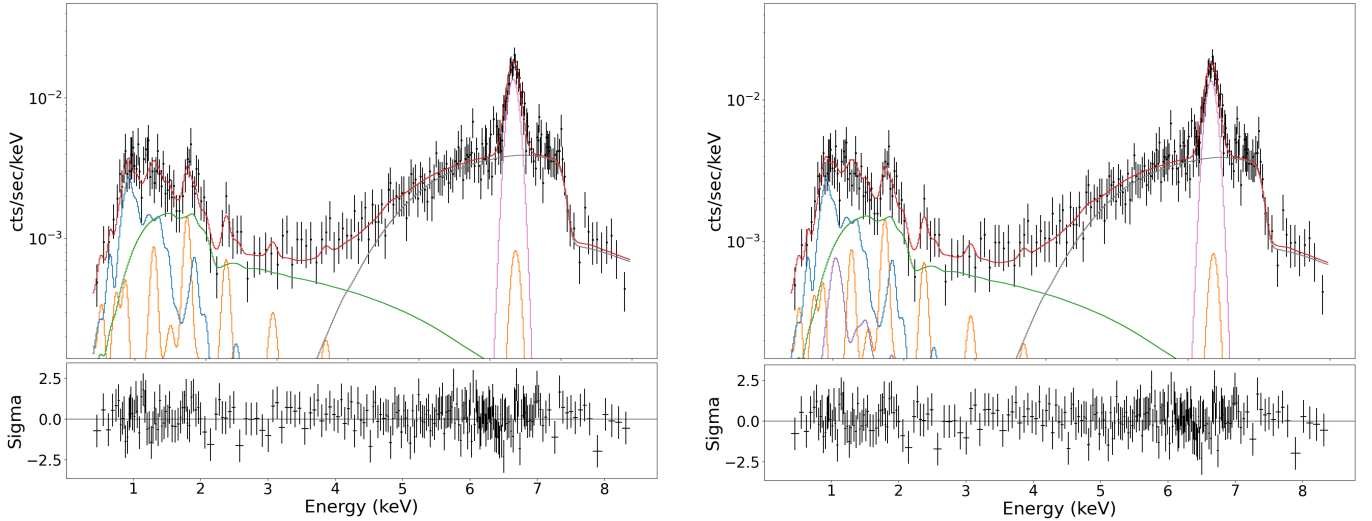


Figure 8. Spectrum from the inner $1.5''$ -radius circle with the best-fit (top) and best-fit residuals (bottom) for a 2-photoionization component model (left) and a 2-photoionization+1-thermal models (right). The hard X-ray spectral fit consists of a Gaussian emission line to model the Fe- $K\alpha$ transition (pink line), and an intrinsically absorbed reflection component `PEXRAV` with $\Gamma = 1.8$ + a cutoff power law (modeling the incident emission) with $\Gamma = 1.8$ (gray line). The soft X-ray emission is best fit with an absorbed power-law component with $\Gamma = 1.5$ (green line), plus 2- photoionization components (blue and orange lines). Adding a third thermal component (purple line, right panel) does not improve the quality of the fit.

5.2.2. The Ionized Bicone

Fig. 2 and 4 clearly show the presence of X-ray emission stretching SE–NW along the bicone direction out to $\sim 2 \text{ kpc}$ ($10''$) from the nucleus. This emission is particularly prominent in the soft band. Extended soft X-ray emission has been observed in numerous Seyfert 1.5–2 galaxies, spatially correlated with $[\text{O III}] \lambda 5007$ emission (e.g., [Levenson et al. 2006](#); [Fabbiano et al. 2022](#)), suggesting a common origin primarily due to photoionization, and partially to collisional ionization of circumnuclear clouds (e.g., [Wang et al. 2011a](#)). Prominent emission lines below 3 keV , typically observed in CT Seyferts ([Wang et al. 2011c](#);

Fabbiano et al. 2017; Maksym et al. 2019), are also present in the analyzed bicone spectra, including Ne IX, Mg XII, and Si XIII. Given the ACIS spectral resolution, these lines are typically blended in the observed spectra.

Fig. 5 and 6 show that the bicone emission is also present at energies >3 keV. Harder extended components (in both the continuum emission above 3 keV and the neutral 6.4 keV Fe $K\alpha$ line) have been detected with *Chandra* in AGNs (e.g., Fabbiano et al. 2017). Table 2 gives the excess counts over the PSF in each conical sector for different energy bands.

For each spectrum, we fit the continuum with a power-law component ($\Gamma = 1.5$ for both regions, with intrinsic absorption $N_H=4.4 \times 10^{20}$ cm $^{-2}$ for the NW cone). The prominent emission lines can be fitted with the addition of redshifted ($z=0.00932$) Gaussians (nine to the NW cone spectrum, ten to the SE cone spectrum), as listed in Table 5. The phenomenological fit returns $\chi^2 \sim 0.27$, and 0.85, for the NW and SE bicone, respectively. Significant residuals can be seen to the left and right of the 6.4 Fe $K\alpha$ line.

As before, we also examined the physical mechanisms responsible for the X-ray emission in the extended conical regions. We initially fit the spectra with a single physical component, adding additional components as necessary. The NW cone is best fit with a 2- photoionization + 2- thermal model. A 2- photoionization component model also returns a good fit but fails to fit the emission ~ 1.0 keV. All models (single and/or multi-component models) fail to fit the emission detected at ~ 6 keV to the red of the neutral Fe $K\alpha$ line.

The SE cone exhibits similar features to the NW cone spectrum, except for a less intense emission peak at ~ 2 keV and a less prominent Fe $K\alpha$ emission line. Fitting all the emission lines requires at least 1- photoionization component + 1- thermal component. Using photoionization *or* thermal models only fails to fit emission ~ 1.3 keV and below 1 keV, as shown in Fig. 10.

In Fig. 11, we compare the low and high ionization parameters (U) used to model the spectra from different Seyfert galaxies, including the values from this work. The ionization parameters we obtain for NGC 5728 are compatible with those reported in the literature for the nuclear and bicone regions (e.g., Paggi et al. 2012; Fabbiano et al. 2018; Jones et al. 2021).

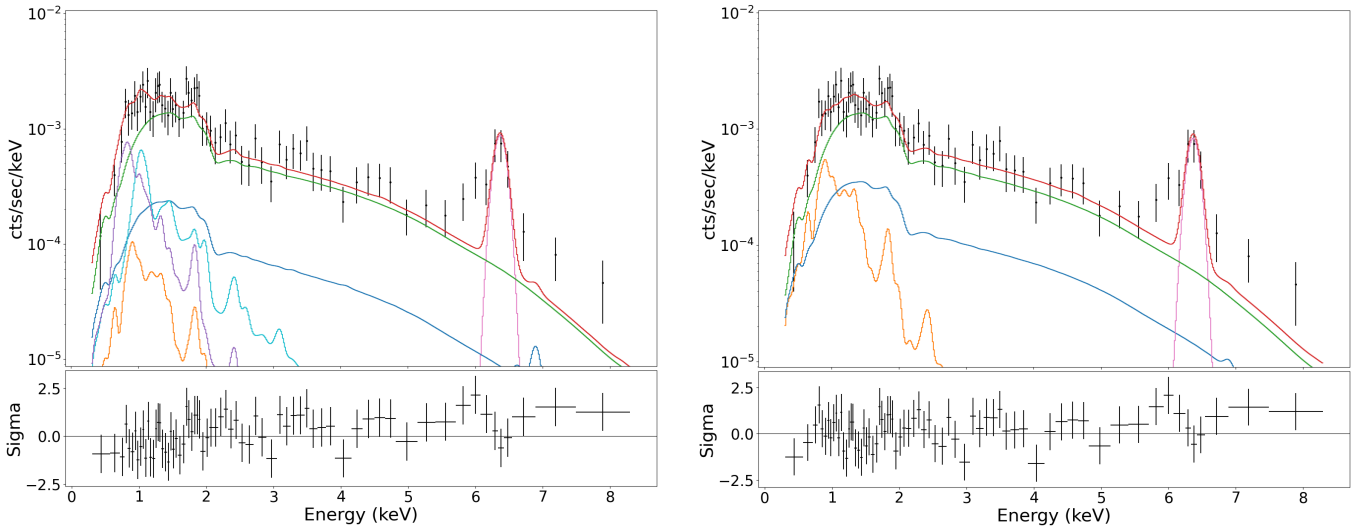


Figure 9. Spectrum from the NW cone region with best-fit (top), and best-fit residuals (bottom). The soft (<3 keV) X-ray emission is best fit with an absorbed power-law component with $\Gamma = 1.5$ (green line), plus a 2- photoionization + 2-thermal models (blue and orange lines, purple and cyan lines, respectively; left panel). The hard (>3 keV) X-ray spectral fit consists of a Gaussian emission line to model the Fe- $K\alpha$ transition (pink line). Even though the soft emission can also be fitted with 2- photoionization model (right panel), the addition of 2- thermal components reduces the residuals < 2 keV.

5.2.3. The Cross Cone Emission

Fig. 4 and Table 2 show significant extended emission in the cross-cone region in the soft band. This emission is evident at energies <3 keV, extending out to a radius of ~ 1.4 kpc ($7''$) from the nucleus, but it is not seen above 4 keV. Therefore, to avoid contamination from the PSF's wings, we analyze the cross-cone emission only in the 0.3-3 keV energy band.

The best phenomenological model for the cross-cone emission consists of an absorbed (intrinsic absorption, $N_H = 4.2 \times 10^{21}$ cm $^{-2}$), steep ($\Gamma=1.3$) power law plus four redshifted ($z=0.00932$) Gaussians. The spectrum still exhibits the strong emission at ~ 1.8 keV observed both in the nuclear and bicone spectra and at ~ 0.9 keV.

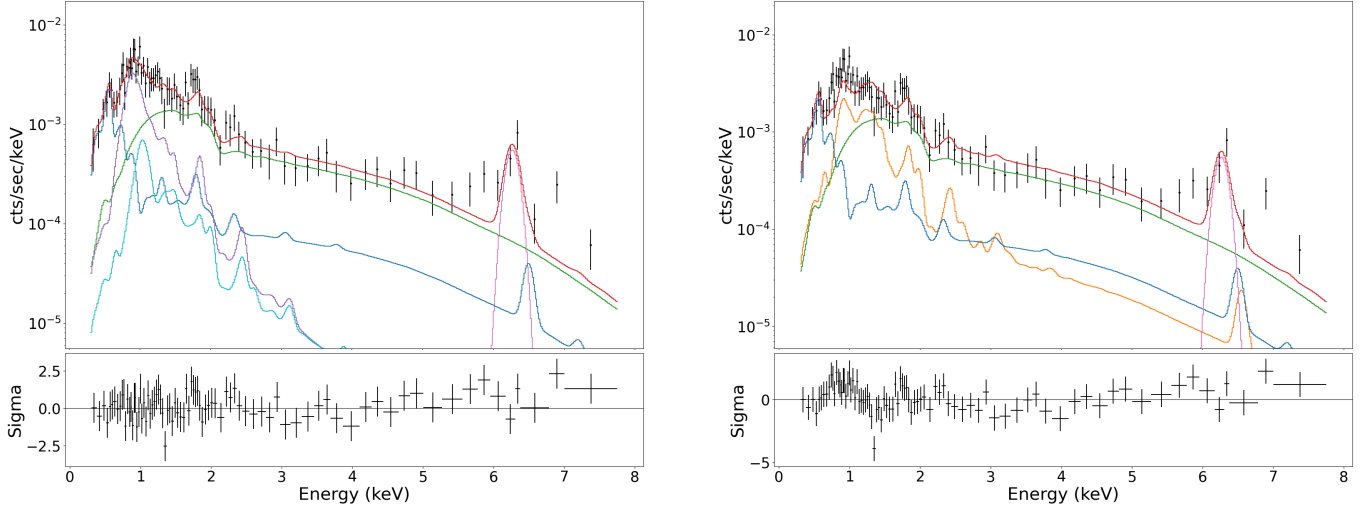


Figure 10. Spectrum from the SE cone region with best-fit (top) and best-fit residuals (bottom). The soft (<3 keV) X-ray emission is best fit with an absorbed power-law component with $\Gamma = 1.5$ (green line), plus a 1- photoionization + 2-thermal models (blue, purple, and cyan lines, respectively; left panel). The hard (>3 keV) X-ray spectral fit consists of a Gaussian emission line to model the Fe-K α transition (pink line). Even though the soft emission can also be fitted with 2- photoionization model (right panel), the addition of thermal components to the 1- photoionization model reduces the residuals < 2 keV and returns the best reduced χ^2 .

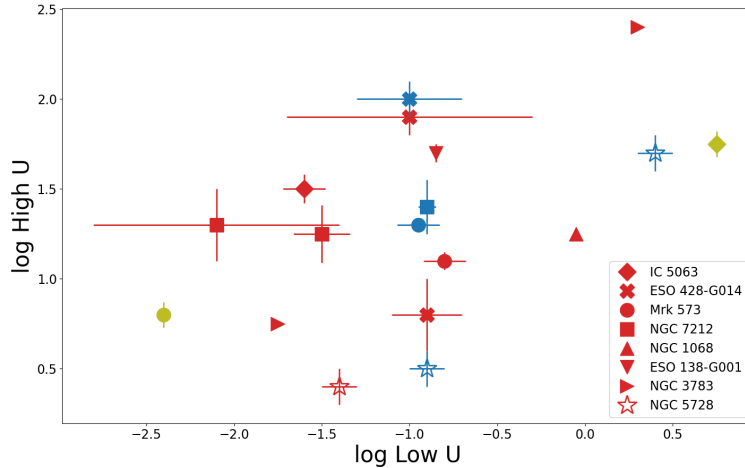


Figure 11. Comparison between the low (x-axis) and high (y-axis) ionization parameters for the best-fit models for NGC 5728 (stars) and the best-fit parameters derived for other Seyfert galaxies from the literature. The icons in red represent the values for the ionization parameters for the nuclear region, blue icons represent the values in the bicone, and green icons the values in the cross-cone direction. The numbers for the best-fit parameters for the Seyfert galaxies in the plot were obtained from [Travascio et al. 2021](#) (IC 5083), [Fabbiano et al. 2018](#) (ESO 428-G014), [Paggi et al. 2012](#) (Mrk 573), [Jones et al. 2020](#) (NGC 7212), [Kraemer et al. 2015](#) (NGC 1068), [De Cicco et al. 2015](#) (ESO-138-G001), and [Blustin et al. 2002](#) (NGC 3783).

The cross-cone spectrum can be best fit with at least 1- photoionization + 1- thermal components. The photoionization component has $\log U \sim 0.3$ and column density $\log (NH) = 23.3 \text{ cm}^{-2}$. Fig. 12 shows that single-component alternative models, such as 1- photoionization (Fig. 12, right panel), fail to fit the emission at ~ 0.7 keV. We opt not to show the results of the best-fit models for the cross-cone emission in Tables 3 and 5 since the number of counts present in the spectrum is not enough to obtain a reliable fit with good statistics.

Fig. 4 shows that the radial profile in the cross-cone direction presents two "bumps" (one in the NE cross-cone and the other in the SW cross-cone) in the 0.3-1.5 keV band. These features can be easily identified in the 0.3-1.5 keV image as arch-like

structures at ~ 1 kpc from the nucleus, consistent with the location of the star-forming ring detected by [Durré & Mould \(2019\)](#) in this object. We will explore these features more fully in a subsequent paper.

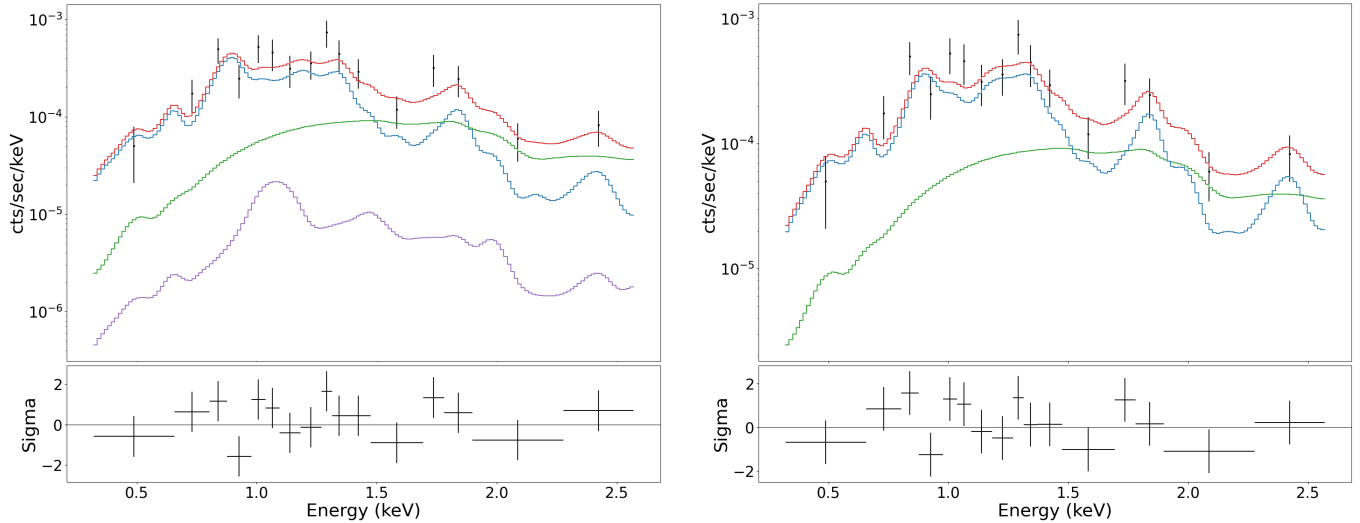


Figure 12. Spectrum for the cross-cone region with best-fit (top) and best-fit residuals (bottom). The soft (< 3 keV) X-ray emission is best fit with an absorbed power-law component with $\Gamma = 1.3$ (green line), plus a 1- photoionization + 1- thermal model (blue and purple lines, respectively; left panel). Even though the soft emission can also be fitted with different single-component models (right panel), adding a thermal and/or photoionization component improves the reduced χ^2 .

5.2.4. Unidentified Spectral Features

As reported in [Table 5](#), we find three unusual emission features in AGN X-ray spectra. The first feature is characterized by emission at ~ 2.8 keV, which is observed in both cone emission spectra. As in [Jones et al. \(2020\)](#), we suggest the identification of this line as being an argon fluorescence line ($E_{\text{lab}} = 2.96$ keV).

We also detect emission features at ~ 3.5 keV in all regions and at 4.5 keV in the NW and SE cone regions. Possible identifications for these lines include Ca $K\alpha$ fluorescence line ($E_{\text{lab}} = 3.69$), and Ar XVII ($E_{\text{lab}} = 3.69$). These lines have been previously observed by [Jones et al. \(2020\)](#) in NGC 7212, another nearby ($z = 0.0266$) CT AGN.

We find two distinct emission lines near 6 and 7 keV, which are observed in the nuclear, NW cone, and SE cone spectra. These features appear as residual excess "wings" redward and blueward of the neutral Fe $K\alpha$ emission line in [Fig. 8, 9, and 10](#). In the physically motivated models, the "blue wing" is partially modeled by high photoionization components as Fe XXV 6.7 keV emission, but with significant fit residuals, as shown on the bottom panels of [Fig. 9, and 10](#). On the other hand, the "red wing" feature cannot be modeled by any combination of photoionization and/or thermal models and appears as excesses in all fits. Similar features have been recently reported in *Chandra* ACIS imaging spectroscopy of the nucleus of the Seyfert 2 Galaxy Mrk 34 ([Maksym et al. 2023](#)). In [Trindade Falcão et al. 2023](#), we conducted a detailed analysis of this unmodeled emission in the bicone. Based on the count excess over the best-fit model, we estimate that, in this region, the feature to the [left, right] of the neutral Fe $K\alpha$ line has $[6.5\sigma, 5.3\sigma]$ significance, with an equivalent width = [1.76 keV, 2.60 keV]. A likelihood ratio test based on a simulation with 100,000 iterations yields a probability $p < 1 \times 10^{-5}$ that a simple power-law continuum plus narrow Fe $K\alpha$ line is a better representation of the data than a model that includes the wings emission.

6. DISCUSSION

Recent studies on obscured AGNs (e.g., [Fabbiano et al. 2017](#); [Jones et al. 2020](#); [Travascio et al. 2021](#)) have produced important and surprising results, revealing extended X-ray emission in both soft X-rays and in the hard energy band, i.e., > 3 keV. These have also enforced the importance of deep ACIS-S *Chandra* observations, with high-resolution (sub-pixel), to obtain an overall picture of the AGN-galaxy interaction and its effects in the ISM.

To further our understanding of the relationship between AGNs and their host galaxy, we conducted a detailed analysis of the soft and hard X-ray emissions in NGC 5728. Below, we discuss the implications of our imaging and spectral analysis.

6.1. Extent as a Function of Energy

In [Fabbiano et al. \(2017\)](#), the authors reported that the extent of the X-ray emission in ESO 428-G014 increases with decreasing photon energy. They suggested that this phenomenon might be caused by a larger concentration of dense molecular clouds in the central region since these clouds are responsible for scattering and reflecting the high-energy photons from the nucleus in the galaxy disk. The same effect was confirmed in more recent studies by [Jones et al. \(2020\)](#); [Travascio et al. \(2021\)](#); [Jones et al. \(2021\)](#).

To measure the full extent of the diffuse emission, we followed the approach adopted in [Fabbiano et al. 2017](#) to measure the width at which the background-subtracted surface brightness (from the radial profiles shown in Fig. 4, 5, and 6) is consistent with the background surface brightness in the same energy band. This corresponds to 1% surface brightness of the peak emission in each energy bin, and errors are primarily due to the uncertainty derived from the bin sizes. This method has been validated by several works (e.g., [Fabbiano et al. 2018](#); [Jones et al. 2020](#); [Travascio et al. 2021](#); [Jones et al. 2021](#)), proving itself to be a reliable comparison of the effective emission extent as a function of energy since the radial profiles have good statistics significance at this surface brightness percentage.

Fig. 13 shows a comparison between the large-scale extent of the emission in NGC 5728 in different energy bands, with that of other CT AGN, reported in the literature ([Fabbiano et al. 2018](#); [Jones et al. 2021](#)). To facilitate the comparison, we normalized the extent of the emission in these sources to that in the soft band and used a simple line model to get the slopes of each extent-energy relation. The energy profile for NGC 5728 shows an overall trend of decreasing FWHM with increasing energy in the cone direction, as for the other analyzed AGN, but also in the cross-cone direction, unlike most other targets plotted. In the cross-cone direction (right panel), there is a decrease of the FWHM, going from 10.1", at the lowest energies, to 9.0" at ~ 3.5 keV (before normalization). Because the emission in this work is consistent with the PSF in the cross-cone direction for energies between 4-7 keV, we opt not to plot these values. In the cone direction (left panel), the FWHM decreases from 14" at the lowest energies to 4.7" at ~ 7 keV (before normalization).

The dependence of the emission extent with energy observed in Fig. 13 can be related to the abundance of high-density ISM clouds near the AGN and the orientation of the ionization bicone with respect to the host galaxy, as the bicone itself originates from the interaction of ionizing photons with the ISM in the host galaxy disk. Soft X-rays are thought to originate as a consequence of photoionization of the ISM and/or collisional ionization when a jet is present (e.g., [Paggi et al. 2012](#)). In contrast, the origin of hard X-rays lies in the interaction between dense ISM clouds and photons from the AGN (e.g., [Reynolds 1997](#)). Our findings show that the soft emission in NGC 5728, as in the other AGN considered, extends farther than the hard emission in the cone direction (Fig. 13, left panel), which suggests a radial dependence on the density and size of the ISM molecular clouds near the AGN, such as a higher prevalence of optically thicker clouds closer to the nucleus ([Fabbiano et al. 2018](#)).

If the ionization bicone is completely aligned with the disk of the galaxy, one would expect to see a radial dependence of the emission extent with energy in the cone direction, as observed in the left panel, but no dependence in the cross-cone direction, since the photons from the AGN do not interact with the ISM clouds at larger radii (in the Unified Model picture). Similarly, if the ionization bicone is perpendicular to the galaxy disk, one would expect no dependence in the cone direction. Even though it is possible for the cross-cone to exhibit some radial energy dependence in this scenario, this emission would be attenuated by the torus. In the case of NGC 5728 and NGC 3393, there is energy radial dependence in the cross-cone *and* cone directions, which could be explained if the ionization bicone holds some inclinations with respect to the host disk, such as the photons from the two regions interact with both the ISM at larger radii *and* with the innermost dense clouds.

Following the approach adopted by [Jones et al. \(2021\)](#), we plot the slope of the normalized extent-energy relation vs. black hole and host galaxy properties, such as column density, black hole masses, bolometric luminosity, and host galaxy diameter (Fig. 14). We find little to no correlation between the extent-energy slope and the obscuring column density, black hole mass, and galaxy diameter (Pearson coefficients show a "weak" correlation for cone and cross-cone directions). On the other hand, we find a tendency for the bolometric luminosity in the cross-cone direction, such that the less luminous sources tend to have the soft X-ray extent dominating the extent in the hard band (Pearson coefficient ~ -0.65).

With our deep *Chandra* observations of NGC 5728, we can also determine the relative amount of cross-cone to cone emission in different energy bands. In Table 4, we list the ratio of the X-ray emission counts (cross-cone/cone), for different energy bands, from the 1.5"-8" conical sectors. Regions containing off-nuclear point sources were excluded. Counts are derived by subtracting the normalized model PSF for each energy band. As in ESO 428-G014 ([Fabbiano et al. 2018](#)), the cross-cone emission is more abundant for energies < 1.5 keV and fairly constant for energies > 3 keV.

6.2. Interpretation of the Physical Models

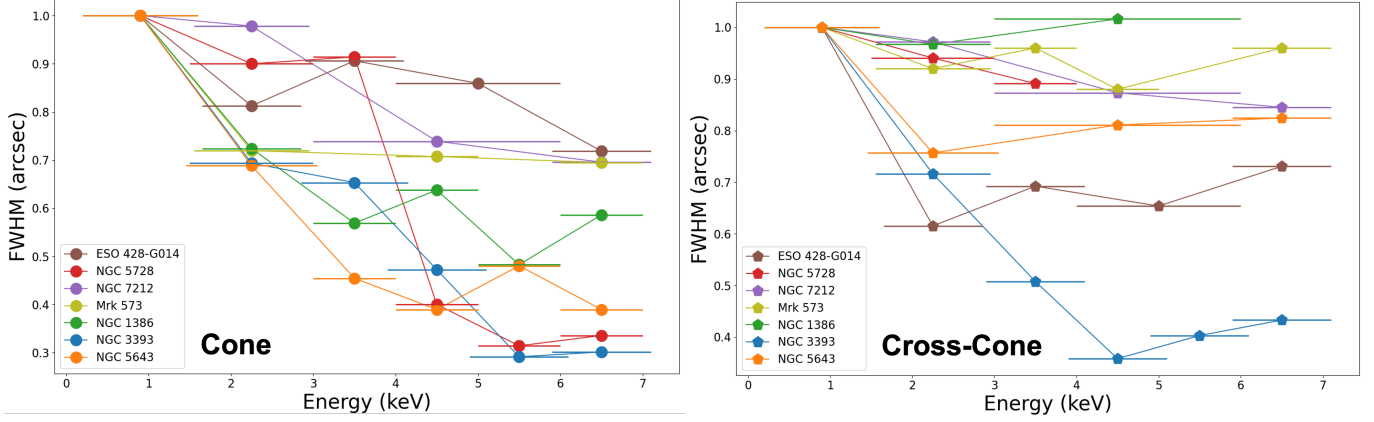


Figure 13. Comparison between the normalized extent in arcsecond at 1% of the surface brightness for NGC 5728 and other CT AGN as a function of energy. The left panel shows the cone direction and the right panel shows the normalized FWHM in the cross-cone direction. Adapted from Fabbiano et al. 2018 and Jones et al. 2021.

Table 4. Extended "Cross-Cone"/"Cone" Emission Ratios

Energy Range (keV)	0.3-3.0	0.3-1.5	1.5-3.0	3.0-6.0	3.0-4.0	4.0-5.0	5.0-6.0
Ratio (error)	Ratio (error)	Ratio (error)	Ratio (error)	Ratio (error)	Ratio (error)	Ratio (error)	Ratio (error)
	0.16 (0.02)	0.20 (0.02)	0.10 (0.01)	0.05 (0.01)	0.04 (0.01)	0.01 (0.01)	0.03 (0.02)

The results of our spectral analysis in Section 5 show that in the central $1.5''$ nuclear region, the best-fit models require at least 2 photoionization components to adequately reproduce emission features over the entire energy range. The addition of a third thermal component with $kT=1.4$ keV is also acceptable (Table 3 and Fig. 8), suggesting that shocks of ~ 1000 - 1200 km/s could be occurring in the central $1.5''$ (300 pc) nuclear region (assuming $v_{shock}^2 = 16k T_{shock}/3\mu$; where k is the Boltzmann constant, and μ is the mean molecular mass of a fully ionized gas; e.g., Fabbiano et al. 2018). The predominance of photoionization processes in the nucleus is supported by the fact that emission of highly ionized species, such as [Si VI] ($1.96\mu\text{m}$), was detected in this object (Durré & Mould 2018) extending out to ~ 300 pc in each direction from the AGN. These emission lines indicate photoionization either from the AGN accretion disk or by fast shocks. The presence of a one-sided radio jet, impacting the gas at about 200 pc from the nucleus (Durré & Mould 2018), may be connected to these shocks, which would have originated from the interaction between the radio jet emission and the ISM. Since the fit statistics are very similar in the central region for different multi-component models (Table 3), both photoionization-only and mixed models are statistically acceptable and probable.

For the emission detected in the bicone, our model results show that 2- thermal components are preferred to fit the spectra from the two cone regions. The APEC output temperatures for the best-fit models ($kT1=0.6\pm 0.15$ and $kT2=1.4\pm 0.27$, for the NW cone; $kT1=0.8\pm 0.11$ and $kT2=1.3\pm 0.11$, for the SE cone) suggest shocks of ~ 700 km/s, 1100 km/s, for the NW cone, and ~ 850 km/s and 1100 km/s, for the SE cone. The thermal components in the cone regions may come from the presence of a radio jet extending in the SE-NW direction or from the interaction between X-ray winds and the ISM (Trindade Falcão et al. 2021b). In the latter case, X-ray outflows that originated close to the AGN entrain small clouds of gas in the ISM, accelerating them to high velocities. In Trindade Falcão et al. 2021b, the authors detect filaments of [O III] gas traveling at ~ 600 km/s and show that shocks with an X-ray wind with velocities ~ 1500 km/s could have caused this acceleration. These velocities are in the same order of magnitude as the shock velocities found in the bicone regions in NGC 5728.

As shown in Table 3, the SE conical region has a higher model flux ($\sim 1.5x$) compared to the NW region, consistent with the fact that the SE cone presents more extended emission than the NW cone in all energy bands. This can be related to the obscuration of the NW X-ray emission by being behind the disk of the galaxy and the star-forming ring (Durré & Mould 2018). Overall, we find that the ionization mechanisms for NGC 5728 are primarily due to AGN activity, with some thermal contribution in the form of shocks in the cones, consistent with the line-ratio diagnostics from Durré & Mould 2018.

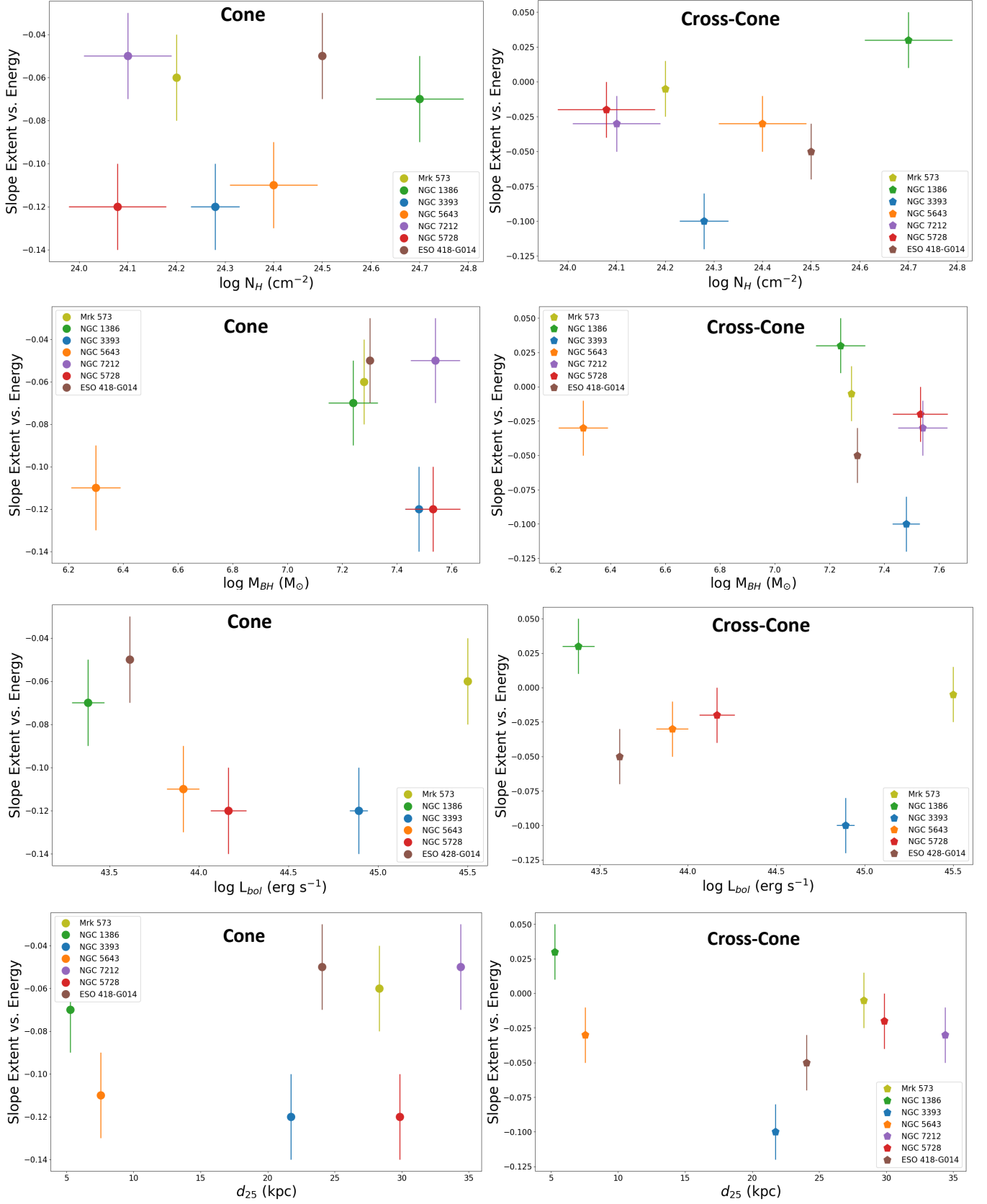


Figure 14. Best-fit slope of the normalized emission extent at 1% of the surface brightness vs. energy in the cone (left column) and cross-cone (right column) regions as a function of (top to bottom): column density, black hole mass, bolometric luminosity, and host galaxy diameter. Adapted from [Fabbiano et al. 2018](#) and [Jones et al. 2021](#).

The photoionization parameters from our best-fit models with `CLOUDY`, i.e., U and NH , can be used to constrain and identify the presence of highly ionized outflows. Conditions in X-ray bicones are similar to those of warm absorbers (WAs) (e.g., Guainazzi et al. 2005). These typically have line-of-sight velocities that range in the 1000-2000 km/s, with $NH \sim 10^{20} - 10^{21} \text{ cm}^{-2}$ (e.g., Fischer et al. 2013), and have, in most cases, originated in the inner 100 pc (e.g., Arav et al. 2015; Krongold et al. 2007).

From Table 3, the photoionization parameters from the nuclear emission are $\log(U1)=0.4$ and $\log(U2)=-1.6$, consistent with what has been found in the literature for 2 phase (high and low ionization components) WA models. For instance, in Kaspi et al. 2002, the authors find that the modeled WAs for NGC 3783 have $\log(U1)=0.8$ (high-velocity component) and $\log(U2)=-1.8$ (low-velocity component). Similarly, in NGC 5548 Andrade-Velázquez et al. (2010) find $\log(U1)=0.7$ (high-velocity component) and $\log(U2)=-0.5$ (low-velocity component). However, the column density of the nuclear low-velocity component is too high ($\sim 100x$ higher) compared to what is observed in these WAs. The NW bicone region, on the other hand, contains a high-velocity ($\sim 1200 \text{ km/s}$) thermal component and U and NH that are more consistent with WAs. In Fig. 15, we plot a comparison between the ionization parameters of 2 phase WAs (or candidates) found in the literature and the values found for NGC 5728 in the NW cone.

The identification and characterization of WA spectral components can be used to construct physical models of these outflowing, highly ionized gas. While we cannot affirm that WAs are present in NGC 5728, the NW cone region is a good candidate to host these high-velocity winds.

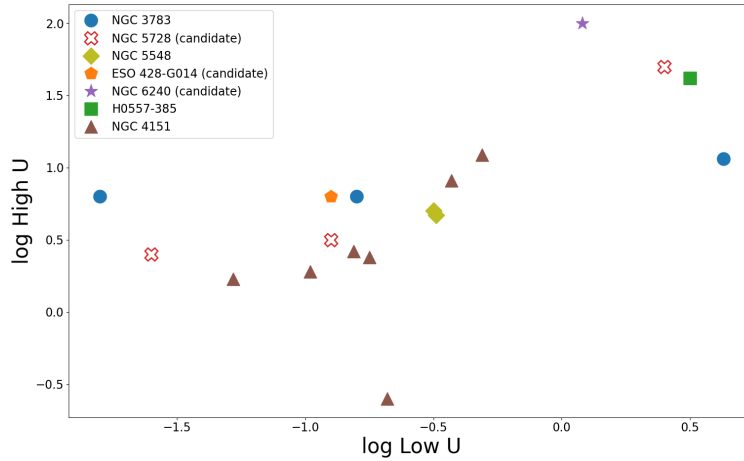


Figure 15. Comparison between the low (x-axis) and high (y-axis) ionization parameters for WAs (and candidates) found in the literature, and our values for the WA candidate found in NGC 5728. The numbers for the best-fit parameters for the Seyfert galaxies in the plot were obtained from Andrade-Velázquez et al. 2010 (NGC 5548), Fabbiano et al. 2018 (ESO 428-G014), Kaspi et al. 2002 (NGC 3783), Krongold et al. 2003 (NGC 3783), Paggi et al. 2022 (NGC 6240), Ashton et al. 2006 (H0557-385), Mizumoto & Ebisawa 2016 (NGC 4051).

6.3. Cone and Cross-Cone Contributions

As discussed in Sections 3 and 5, we detect extended emission in the soft band, both in the cone and cross-cone directions. The NW and SE cones contribute $\sim 34\%$ of the total observed counts (in the broad-band, in a $8''$ radius circle), with the NW cone contributing $\sim 15\%$ and the SE cone $\sim 19\%$. For a $1.5''-8''$ annulus region, the NW cone contributes $\sim 44\%$ and the SE cone $\sim 45\%$, with the cross-cone contributing the remaining $\sim 11\%$ of the total observed counts in the 0.3-7 keV energy band in this region. Regarding the emission below 3 keV, the total contribution of the NW cone is $\sim 22\%$ of the total observed counts in a $8''$ radius, while the SE cone contributes $\sim 33\%$. For a $1.5''-8''$ annulus region, the NW cone contribution is $\sim 46\%$, and the SE cone contribution is $\sim 50\%$. The lower contribution percentage of the NW cone compared to the SE cone might be related to the obscuration caused by the star-forming ring or the host galaxy disk to the NW region, as discussed.

By comparing the extent of the X-ray emission at 1% surface brightness with energy (Fig. 13), we find that both the cone and cross-cone emissions are more extended than the model PSF for energies below 3 keV. For the cross-cone direction, the soft X-rays extend on kpc scales. This emission is detected in a direction where the radiation from the AGN should be obscured by the torus, based on the AGN unification model (Antonucci 1993). The origin of this emission is still unknown, but if it originated in the nuclear region, this radiation is likely produced by the corona and has interacted with the surrounding ISM, propagating to larger radii.

The idea of a "porous", clumpy torus has been suggested by other authors before to explain this excess emission (e.g., Wang et al. 2011c; Fabbiano et al. 2017), which would occur along the plane of the obscuring component. We can estimate the transmission in the cross-cone direction by considering the cone and cross-cone's solid angles (See Section 3). Since the total bicone region volume is ~ 2.5 x larger than that of the cross-cone, the transmission in the cross-cone direction needs to be $\sim 2\%$ of that of the bicone direction. This is lower than the cross-cone transmission estimated for other CT AGN in the literature (e.g., ESO 428-G014 (Fabbiano et al. 2018), $\sim 10\%$; NGC 7212 (Jones et al. 2020), $\sim 16\%$).

Another possibility is that this emission in the cross-cone direction is related to the radio jet seen at 6cm, aligned with the NW-SE bicone emission (e.g., Durré & Mould 2018). The presence of warm and hot emissions due to jet/cold-disk interactions have been modeled using relativistic hydrodynamical simulations (e.g., Mukherjee et al. 2018), and models have shown that gas with temperatures $\sim 10^7$ K may be ejected in the form of winds from the central regions on large scales, surrounding the cooler gas present in these regions. This is consistent with the temperatures found in our best-fit models for the NW and SE cone regions ($kT \sim 10^7$ K ~ 0.9 keV), and best alternative model for the central $1.5''$ region.

Finally, a third possibility is that the origin of this excess extended emission is not related to nuclear activity but emission produced by hot ISM connected with the star-forming ring. Durré & Mould (2018) presented the VLA 20cm radio large-scale map of NGC 5728 and showed that the radio emission exists in the nuclear region and also in two regions coinciding with two regions of star formation at the end of the galaxy bar.

7. CONCLUSIONS

We analyze the deep *Chandra* observation of the CT AGN NGC 5728 to study the kpc-scale diffuse X-ray emission, both spectrally and spatially, as a function of energy. In summary, our conclusions are as follows:

1. We detect a lower energy total extent of ~ 4 kpc in the direction of the major axis of NGC 5728, which is also the direction of the ionization bicone (Durré & Mould 2018). We find an energy-related trend in the size of the extended emission, with the softer emission (< 3 keV) being more extended than the harder emission. The smaller extent of the hard continuum and Fe $K\alpha$ profiles imply that the optically thicker clouds responsible for this scattering may be relatively more prevalent closer to the nucleus. These clouds must not prevent soft ionizing X-rays from the AGN from escaping to larger radii to have photoionized ISM at larger distances. Therefore, these scattering clouds must be clumped and have higher density. This suggests that at smaller radii, there may be a larger population of molecular clouds to scatter the hard X-rays, as in the Milky Way (e.g., Nakanishi & Sofue 2006);

2. The diffuse emission is also extended in the cross-cone direction, where the AGN emission would be mostly obscured by the torus in the standard AGN model. The presence of hard X-rays detected on kpc scales suggests a non-uniform, clumpy torus structure (e.g., Nenkova et al. 2008), which allows the radiation to escape from the circumnuclear region to larger radii. If this is the case, we estimate that the transmission in the cross-cone direction is $\sim 2\%$ of the bicone direction. This is lower than the transmission found by Fabbiano et al. (2018) for ESO 428-G014 ($\sim 10\%$), and by Jones et al. (2020) for NGC 7212 ($\sim 16\%$);

3. We show that the extent as a function of energy at 1% of the surface brightness in the cone region of NGC 5728 exhibits a steeper relationship than the cross-cone region. This may be explained by an inclination effect, in which the orientation of the ionization bicone with respect to the host disk molecular clouds impacts the extent to which the soft X-rays propagate through the ISM. We also compare the energy-extent slopes to galaxy and black hole properties and find for the cross-cone that the lower luminosity targets tend to have the soft X-rays extending farther than the hard X-rays.

4. We extract the spectrum from four different regions: a $1.5''$ (300 pc) nuclear region, two $1.5''$ - $8''$ (300 - 1600 pc) conical sectors, namely SE and NW bicone, and one $2''$ - $8''$ (400 - 1600 pc) conical region, namely cross-cone. Using a nuclear `PEXRAV + XSZCUTOFFPL` model to represent the reprocessed emission (for the nuclear fit only) + additional power-law to fit the soft emission and a set of Gaussian lines (e.g. Levenson et al. 2006), we separately analyzed the emission in these regions. The model fits suggest the presence of blended O VII, O VIII, Ne IX, Ne X, and several Fe lines at energies < 1.2 keV in these regions. We also detect more isolated emission from lines that can be identified as Mg (XI, XII), and Si, which is consistent with the findings in other AGN (e.g., Koss et al. 2015; Fabbiano et al. 2018; Traverscio et al. 2021);

5. As reported by Fabbiano et al. (2017) for the soft component, all these spectral components are associated with large-scale spatial components, although point-like nuclear emission can also be seen at the higher energies and in the Fe $K\alpha$ line. The observed continuum emission in the $1.5''$ - $8''$ annulus accounts for $\sim 39\%$ of the total observed continuum in the 0.3-7 keV band. In the hard band (3.0-7.0 keV), 19% of the continuum is observed in the $1.5''$ - $8''$ annulus;

6. We detect 4 emission features that are not typical of CT AGN. The emission lines at ~ 2.8 keV, and ~ 3.5 keV were tentatively identified as Ar $K\alpha$ (2.9 keV), Ar XVII (3.7 keV), and Ca $K\alpha$ (3.7 keV). The emission features to the red (~ 6.1 keV) and to the blue (~ 6.8 keV) of the 6.4 Fe $K\alpha$ line, are observed in the spectra extracted from all three regions, but could not be entirely identified;

7. We fit the spectra with photoionization and/or thermal models. In the inner 1.5'' circumnuclear region, the spectrum is best fit with a minimum of 2-photoionization components, although adding a third thermal component is also acceptable. For the conical regions, the NW and SE cones are best fit with at least 1- photoionization + 1- thermal components, although 2-photoionization + 2- thermal components are preferred for the NW conical region;

8. Physical interpretation of our fitting results suggests that the best-fit thermal components for NGC 5728 can be explained by ISM interactions, shocks, or supernova remnants/star formation from the nearby star-forming ring. Specifically:

- In the inner 1.5'' central region, the alternative model fit suggests temperatures of ~ 1.4 keV, resulting in ~ 1000 - 1100 km/s shocks. For the extended emission (1.5''-8'' conical regions), the thermal components have similar temperatures compared to those of the nuclear region, ~ 1.4 keV and 1.3 keV, corresponding to shocks ~ 1100 - 1200 km/s.

-The lower temperature components in the cone regions (kT ~ 0.6 - 0.8) can also be explained by jet-ISM interactions. In this case, cool gas in the nucleus is surrounded by warm gas in the central region, with the latter being ejected from the nucleus on large scales in the form of winds.

-The possibility of supernova heating and/or heating from star-forming regions is not ruled out. We will further explore this possibility in a subsequent paper;

9. We find that our models' ionization parameters for the inner 1.5'' emission are consistent with those found in warm absorbers (WAs). However, the typical column densities values for WAs are more consistent with the parameters obtained for the preferred model in the NW cone region rather than in the very central source;

This paper demonstrates how deep *Chandra* observations can produce surprising results on "standard" sources, recovering crucial information about the AGN and surrounding ISM. With statistically significant spectral and spatial information, these observations have uncovered large-scale diffuse X-ray emission and have allowed us an opportunity to study and test the AGN standard model, providing new insights into the physics of AGN and AGN feedback.

1 The authors thank the anonymous referee for helpful comments that improved the clarity of this paper. We thank Margarita
2 Karovska and Steve Kraemer for their valuable comments on the manuscript. This work was partially supported by NASA
3 contract NAS8-03060 (CXC) and the *Chandra* Guest Observer program grant GO0-21094X (PI: Fabbiano). The NASA ADS
4 bibliography service was used in this work. This research has made use of the NASA/IPAC Extragalactic Database (NED), which
5 is operated by the Jet Propulsion Laboratory, California Institute of Technology, under contract with the National Aeronautics
6 and Space Administration. This work used the photoionization code CLOUDY, and we thank Gary Ferland and associates for the
7 maintenance and development of the software.

REFERENCES

- Andrade-Velázquez, M., Krongold, Y., Elvis, M., et al. 2010, *ApJ*, 711, 888
- Antonucci, R. 1993, *Annual Review of Astronomy and Astrophysics*, 31, 473
- Arav, N., Chamberlain, C., Kriss, G. A., et al. 2015, *Astronomy & Astrophysics*, 577, A37
- Armentrout, B. K., Kraemer, S. B., & Turner, T. J. 2007, *The Astrophysical Journal*, 665, 237
- Ashton, C. E., Page, M. J., Branduardi-Raymont, G., & Blustin, A. J. 2006, *Monthly Notices of the Royal Astronomical Society*, 366, 521
- Baloković, M., Brightman, M., Harrison, C. M., et al. 2018, *ApJ*, 854, 42
- Blustin, A. J., Branduardi-Raymont, G., Behar, E., et al. 2002, *A&A*, 392, 453
- Dasyra, K. M., Combes, F., Oosterloo, T., Oonk, J. B. R., et al. 2016, *Astronomy & Astrophysics*, 595, L7
- De Cicco, M., Marinucci, A., Bianchi, S., et al. 2015, *Monthly Notices of the Royal Astronomical Society*, 453, 2155
- Di Matteo, T., Springel, V., & Hernquist, L. 2005, *Nature*, 433, 604
- Durré, M., & Mould, J. R. 2018, *ApJ*, 867, 149
- . 2019, *ApJ*, 870, 37
- Fabbiano, G., Elvis, M., Paggi, A., et al. 2017, *The Astrophysical Journal Letters*, 842, L4.
<https://dx.doi.org/10.3847/2041-8213/aa7551>
- Fabbiano, G., Paggi, A., Karovska, M., et al. 2018, *ApJ*, 855, 20
- Fabbiano, G., Paggi, A., Morganti, R., et al. 2022, *ApJ*, 938, 16
- Ferland, G. J., Chatzikos, M., Guzmán, F., et al. 2017, *Revista Mexicana de Astronomía y Astrofísica*, 49, 1379
- Fischer, T. C., Crenshaw, D. M., Kraemer, S. B., & Schmitt, H. R. 2013, *The Astrophysical Journal*, 209, 1
- Foster, A. R., Smith, R. K., & Brickhouse, N. S. 2012, *ApJ*, 756, 128
- Freeman, P., Doe, S., & Siemiginowska, A. 2001, *SPIE Proceedings*, 4477, 76

- Fruscione, A., McDowell, J. C., Allen, G. E., et al. 2006, in *Observatory Operations: Strategies, Processes, and Systems*, ed. D. R. Silva & R. E. Doxsey, Vol. 6270
- Guainazzi, M., Matt, G., & Perola, G. C. 2005, *A&A*, 444, 119
- Jones, M. L., Fabbiano, G., Elvis, M., et al. 2020, *ApJ*, 892, 133
- Jones, M. L., Parker, K., Fabbiano, G., et al. 2021, *ApJ*, 910, 26
- Kaspi, S., Brandt, W. N., George, I. M., et al. 2002, *ApJ*, 574, 643
- Koss, M., Trakhtenbrot, B., Ricci, C., et al. 2017, *ApJ*, 850, 31
- Koss, M., Romero-Cañizales, C., Baronchelli, L., et al. 2015, *ApJ*, 807, 18
- Kraemer, S. B., Sharma, N., Turner, T. J., & George, I. M. Crenshaw, D. M. 2015, *The Astrophysical Journal*, 798, 53
- Kraemer, S. B., Turner, T. J., Couto, J. D., et al. 2020, *Monthly Notices of the Royal Astronomical Society*, 493, 3893
- Krolik, J., Madau, P., & Zycki, P. 1994, *ApjL*, 420, L57
- Krongold, Y., Nicastro, F., Brickhouse, N. S., et al. 2003, *ApJ*, 597, 832
- Krongold, Y., Nicastro, F., Elvis, M., et al. 2007, *ApJ*, 659, 1022
- Levenson, N. A., Heckman, T. M., Krolik, J. H., Weaver, K. A., & Życki, P. T. 2006, *ApJ*, 248, 111
- Magdziarz, P., & Zdziarski, A. 1995, *Monthly Notices of the Royal Astronomical Society*, 273, 837
- Maksym, P., Elvis, M., Fabbiano, G., et al. 2023, arXiv:2209.14326
- Maksym, W. P., Fabbiano, G., Elvis, M., et al. 2019, *The Astrophysical Journal*, 872, 94
- Mizumoto, M., & Ebisawa, K. 2016, *Monthly Notices of the Royal Astronomical Society*, 466, 3259
- Morganti, R., Holt, J., Saripalli, L., Oosterloo, T., & Tadhunter, C. N. 2007, *Astronomy & Astrophysics*, 476, 735
- Mould, J. R., Huchra, J. P., Freedman, W. L., et al. 2000, *ApJ*, 529, 786
- Mukherjee, D., Wagner, S. J., Bicknell, G. V., et al. 2018, *Monthly Notices of the Royal Astronomical Society*, 476, 80
- Nakanishi, H., & Sofue, Y. 2006, *Monthly Notices of the Royal Astronomical Society*, 58, 847
- Nenkova, M., Sirocky, M. M., Nikutta, R., Ivezić, Z., & Elitzur, M. 2008, *ApJ*, 685, 160
- Paggi, A., Fabbiano, G., Nardini, E., et al. 2022, *ApJ*, 927, 20
- Paggi, A., Wang, J., Fabbiano, G., Elvis, M., & Karovska, M. 2012, *ApJ*, 756, 39
- Porter, R. L., Ferland, G. J., Kraemer, S. B., et al. 2006, *PASP*, 118, 920
- Reynolds, C. S. 1997, *Monthly Notices of the Royal Astronomical Society*, 286, 513
- Semena, A. N., Sazonov, S. Y., & Krivonos, R. A. 2019, *Astronomy Letters*, 45, 490
- Shu, X. W., Wang, J. X., Jiang, P., Fan, L. L., & Wang, T. G. 2007, *The Astrophysical Journal*, 657, 167. <https://dx.doi.org/10.1086/510579>
- Silk, J., & Rees, M. J. 1998, *Astronomy and Astrophysics*, 331, L1
- Tanimoto, A., Ueda, Y., Odaka, H., Yamada, S., & Ricci, C. 2022, *ApJ*, 260, 30
- Travascio, A., Fabbiano, G., Paggi, A., et al. 2021, *ApJ*, 921, 129
- Trindade Falcão, A., Fabbiano, G., Elvis, M., Paggi, A., & Maksym, W. P. 2023, *ApjL*
- Trindade Falcão, A., Kraemer, S. B., Fischer, T. C., et al. 2021a, *Monthly Notices of the Royal Astronomical Society*, 500, 1491
- , 2021b, *Monthly Notices of the Royal Astronomical Society*, 505, 3054
- Urry, C. M., & Padovani, P. 1995, *Astronomical Society of the Pacific*, 107, 803
- Wang, J., Fabbiano, G., Elvis, M., et al. 2011a, *The Astrophysics Journal*, 736, 62
- Wang, J., Fabbiano, G., Risaliti, G., et al. 2011b, *The Astrophysics Journal*, 729, 75
- Wang, J., Fabbiano, G., Elvis, M., et al. 2011c, *The Astrophysics Journal*, 742, 23
- Wilson, A. S., Braatz, J. A., Heckman, T. M., Krolik, J. H., & Miley, G. K. 1993, *Astrophysical Journal Letters*, 419, L61

APPENDIX

A. ALTERNATIVE FITTING MODELS

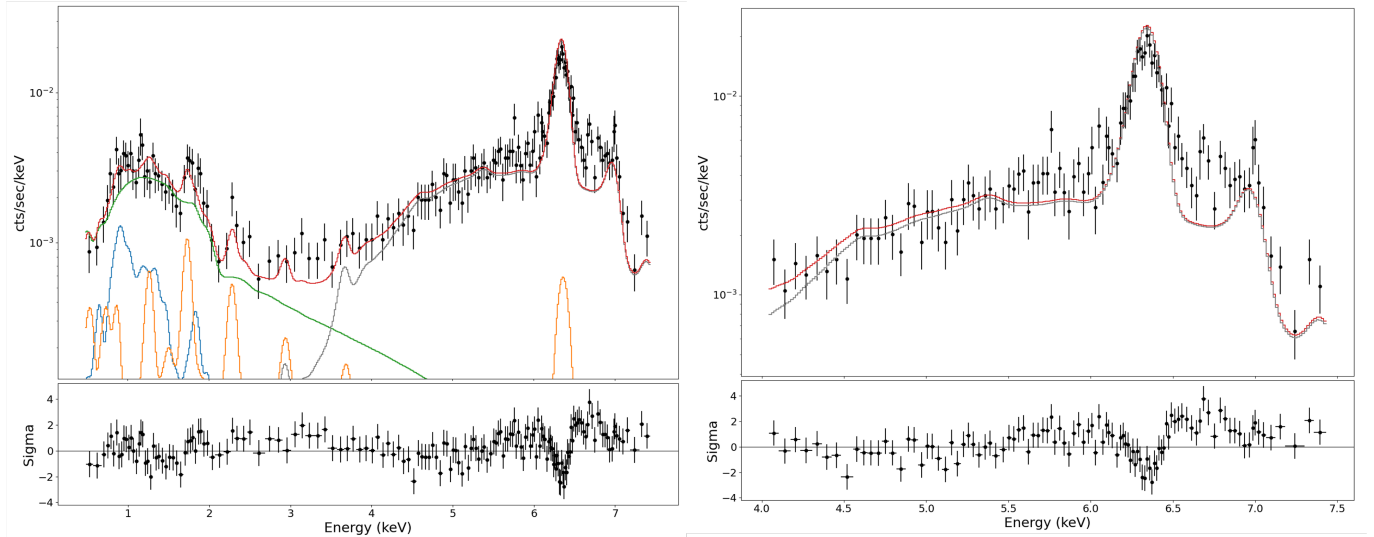


Figure 16. **Left:** Full-band (0.3-8 keV) spectrum from the inner 1.5''-radius circle with the best-fit (top) and best-fit residuals (bottom) for a 2-photoionization component model. The hard X-ray spectrum was fit with `BORUS02` with $\Gamma=2.1$ (in gray). As shown, the excess emission seen to the left and right of the neutral Fe $K\alpha$ still appears as residuals at ~ 6 and 7 keV. **Right:** Hard (4-8 keV) spectrum from the inner 1.5''-radius circle with the best-fit `BORUS02` model (top) and best-fit residuals (bottom), shown in more detail.

We fit the hard nuclear spectrum with `BORUS02` (Baloković et al. 2018), as an alternative model for `PEXRAV+XSZCUTOFFPL`. The reprocessed component represented by this model is produced by the obscuring material near the SMBH, and it includes the scattered component and fluorescent lines (see the `BORUS02` website¹⁶ for details). We fixed the energy cutoff at 200 keV, and assumed the cosine of the angle at which the observer looks at the plane layer to be $\cos(\theta)=0.5$ (e.g., Semena et al. 2019). The results of this analysis are shown in Fig. 16. The best-fit model for this torus component returns a photon index $\Gamma=2.1\pm 0.3$, and hydrogen column density component $\log N_{\text{H}}=23.8\pm 0.1$. As shown, excess emission redward and blueward of the neutral Fe $K\alpha$ line is still observed in the bottom panels, near 6 and 7 keV.

B. EMISSION LINES IDENTIFICATION

Table 5. Spectral Fitting Results for the Extracted Spectra

Region	Counts (error) (0.3-7.0 keV)	Norm. Po. Law ($\text{ph cm}^{-2} \text{s}^{-1}$)	Model Energy Flux (0.3-7.0 keV; in $\text{erg/cm}^2/\text{s}$)	χ^2
(1.5'' circle)	4577 (67)	4.0×10^{-6}	2.5×10^{-12}	0.69
(1.5'' - 8'' NW Bicone)	1091 (28)	6.0×10^{-6}	7.2×10^{-14}	0.27
(1.5'' - 8'' SE Bicone)	1383 (32)	6.0×10^{-6}	1.1×10^{-13}	0.85
Emission Lines:				
Observed Energy (keV)	Flux ($10^{-6} \text{ ph cm}^{-2} \text{ s}^{-1}$)	Identification (E_{lab} keV) ^a		
(1.5'' circle)	(1.5'' circle)			
(1.5'' - 8'' NW Bicone)	(1.5'' - 8'' NW Bicone)			
(1.5'' - 8'' SE Bicone)	(1.5'' - 8'' SE Bicone)			

¹⁶ <http://www.astro.caltech.edu/mislavb/download/>

-	-	*O VII (0.57)
-	-	
0.46±0.08	49.1±18.5	
-	-	
0.73±0.05	3.4±1.2	*Fe XVII (0.83)
0.76±0.01	5.0±0.01	
0.82±0.01	4.83±0.72	*O VIII (0.65),
-	-	*Fe XVII (0.83)
-	-	
-	-	*Ne IX (0.90),
-	-	*Fe XIX (0.92)
0.90±0.02	7.40±1.16	
0.98±0.01	2.41±0.3	*Fe XXI (1.01),
0.99±0.07	2.13±0.73	*Ne X (1.02)
-	-	
1.17±0.01	1.35±0.21	*Fe XXIV (1.13, 1.17)
-	-	
1.18±0.03	1.29±0.36	
1.33±0.01	1.05±0.28	Mg XI (1.33)
-	-	
-	-	
1.75±0.01	0.58±0.12	Si XIII (1.84)
1.82±0.05	0.43±0.15	
1.79±0.02	0.38±0.14	
1.92±0.02	0.43±0.11	Si XIII (1.86)
-	-	
-	-	
2.32±0.02	0.49±0.14	S K α (2.31),
2.32±0.06	0.42±0.18	S XV (2.43)
2.35±0.03	0.37±0.15	
-	-	Ar K α (2.96) [★]
2.76±0.08	0.11±0.09	
2.95±0.06	0.15±0.08	
3.14±0.05	0.17±0.09	Ar XVII (3.69) [★] ,
3.54±0.11	0.39±0.16	Ca K α (3.69) [★] ,
3.61±0.06	0.18±0.11	blend of line
-	-	Ca K α (3.69) [★] ,
4.65±0.08	0.26±0.12	blend of lines
4.49±0.17	0.49±0.18	
-	-	Fe K α "Red Wing" [★]
6.30±0.12	1.73±0.39	
-	-	
6.40±0.01	18.02±0.91	Fe K α (6.44 keV)
6.45±0.04	0.69±0.26	
6.33±0.04	0.83±0.23	

^a Energies from NIST; [Koss et al. 2015](#); [Maksym et al. 2019](#); [Travascio et al. 2021](#).

* Lines blended in the ASCIS-S spectrum <1.3 keV. These are tentative identifications

★ These lines do not fit into our current understanding of AGN emission.